UCLA
UCLA Previously Published Works

Title

Polycyclic Metamorphism, Exhumation, and Recycling of Subduction Complex Rocks, Cedros Island, Baja California

Permalink

https://escholarship.org/uc/item/61g510pn

Journal

Tectonics, 45(4)

ISSN

0278-7407

Authors

Wang, Jordan W
Kapp, Paul
Holder, Robert
et al.

Publication Date

2026-04-01

DOI

10.1029/2025tc009340

Copyright Information

This work is made available under the terms of a Creative Commons Attribution-NonCommercial-ShareAlike License, available at
https://creativecommons.org/licenses/by-nc-sa/4.0/

Peer reviewed

eScholarship.org Powered by the California Digital Library
University of California

Check for updates

ADVANCING EARTH AND SPACE SCIENCES

Tectonics

RESEARCH ARTICLE
10.1029/2025TC009340

Polycyclic Metamorphism, Exhumation, and Recycling of Subduction Complex Rocks, Cedros Island, Baja California

Jordan W. Wang[1,2], **Paul Kapp**[2], **Robert Holder**[3], **John He**[1], **David Hernández-Uribe**[4], and **James Worthington**[2]

[1]Department of Earth, Planetary, and Space Sciences, University of California Los Angeles, Los Angeles, CA, USA, [2]Department of Geoscience, University of Arizona, Tucson, AZ, USA, [3]Department of Earth and Environmental Sciences, University of Michigan, Ann Arbor, MI, USA, [4]Department of Earth and Environmental Sciences, University of Illinois Chicago, Chicago, IL, USA

Key Points:

- Subduction complex rocks are exhumed in the footwalls of normal faults beneath forearc basin strata and attenuated mantle
- High-pressure blocks record $^{40}Ar/^{39}Ar$ ages from 172 to 144 Ma and are hosted in much younger siliciclastic matrix (ca. 92 to 72 Ma)
- Blocks were assembled via multiple cycles of extension and sedimentary recycling back into the subduction trench

Supporting Information:

Supporting Information may be found in the online version of this article.

Correspondence to:

J. W. Wang,
jordanww@epss.ucla.edu

Citation:

Wang, J. W., Kapp, P., Holder, R., He, J., Hernández-Uribe, D., & Worthington, J. (2026). Polycyclic metamorphism, exhumation, and recycling of subduction complex rocks, Cedros Island, Baja California. *Tectonics*, *45*, e2025TC009340. https://doi.org/10.1029/2025TC009340

Received 18 DEC 2025
Accepted 14 APR 2026

Author Contributions:

Conceptualization: Jordan W. Wang, Paul Kapp, Robert Holder, David Hernández-Uribe, James Worthington
Data curation: Jordan W. Wang
Funding acquisition: Paul Kapp, Robert Holder, David Hernández-Uribe, James Worthington
Investigation: Jordan W. Wang, Paul Kapp, Robert Holder, John He, David Hernández-Uribe, James Worthington
Methodology: Jordan W. Wang

© 2026. The Author(s).
This is an open access article under the terms of the Creative Commons Attribution-NonCommercial-NoDerivs License, which permits use and distribution in any medium, provided the original work is properly cited, the use is non-commercial and no modifications or adaptations are made.

Abstract High-pressure rocks from subduction complexes are key records of the physical and chemical processes that operate on the subduction interface, but interpretation of these records requires accurate structural understanding of where they formed in the subduction zone and the mechanisms by which they were exhumed. We present new geologic mapping, outcrop-scale observations, and geochronology from subduction-zone assemblages at Punta Prieta Ridge on Cedros Island, Baja California (Mexico), to investigate the history of subduction, exhumation, and structural assembly of these rocks. The rocks of Punta Prieta Ridge are exposed in the footwalls of high- and low-angle normal faults that carry Cretaceous forearc basin strata and attenuated mantle sections of the Cedros Island Ophiolite in their hangingwalls. The footwall rocks are subduction-zone assemblages organized into distinct nappes that decrease in metamorphic grade and degree of strain structurally downward. Garnet-amphibolite and blueschist blocks within the subduction complex yield $^{40}Ar/^{39}Ar$ cooling ages between 172 and 144 Ma and are hosted in siliciclastic rocks which yield detrital zircon maximum depositional ages between 92 and 72 Ma. Based on field evidence and age relationships, we interpret the occurrence of older higher-grade blocks in younger clastic matrix to be depositional rather than the result of tectonic mixing. We then present a model for their exhumation and assembly via multiple cycles of extensional unroofing of the subduction complex and sedimentary recycling of high-pressure rocks back into the subduction trench. We conclude by comparing the record of subduction on Cedros Island to other parts of the Cordillera.

1. Introduction

High-pressure rocks exhumed in subduction complexes provide first-order insights into the thermomechanical properties of subduction zones (e.g., Agard et al., 2018; Peacock, 1996) and the geodynamic evolution of ancient convergent margin systems (e.g., Isozaki et al., 2010; Wakabayashi, 2015) but remain difficult to interpret due to outstanding questions around their exhumation mechanisms and potential preservation biases (Agard et al., 2009; Penniston-Dorland et al., 2015; van Keken et al., 2018). Over the past 50 years, several mechanisms have been invoked to explain the exhumation of deeply subducted rocks. These mechanisms include (a) underplating of material at the base of the accretionary wedge coupled with rapid surface erosion (Platt, 1975; Ring & Brandon, 1999; Ruh, 2020) and/or brittle-ductile extension in the upper portion of the wedge (Menant et al., 2020; Platt, 1986; Teyssier et al., 2010), (b) buoyancy driven processes due to density contrasts between the subducting crustal materials and surrounding mantle rocks (J. B. Chapman, 2021; England & Holland, 1979; Ernst, 1971; Platt, 1987), (c) corner flow induced by narrowing of a low-viscosity subduction channel at depth (Cloos, 1982; Gerya et al., 2002), and (d) wedge extrusion, where materials along the subduction channel are exhumed via up-dip motion accommodated by basal thrusts and overlying normal faults, either as a rigid wedge along discrete faults (e.g., Maruyama et al., 1996; Wakabayashi, 1999) or in a more distributed fashion along channel flow-type shear zones (e.g., Beaumont et al., 2009). None of these processes are necessarily mutually exclusive, and detailed field studies and numerical models have been published in favor of each of them (see references above), but determining which processes were responsible for rock recovery in specific field contexts remains an important challenge.

The problem of interpreting the correct geodynamic context for high-pressure thermobarometric data is well illustrated in the Franciscan Complex of California, which records a variably incomplete record of Early Jurassic to Paleogene subduction-zone metamorphism, accretion, and deformation concomitant with the main phase of Cordilleran orogenesis in North America. Most of the Franciscan Complex is composed of coherent,

Project administration: Paul Kapp, Robert Holder, David Hernández-Uribe, James Worthington
Supervision: Jordan W. Wang, Paul Kapp, Robert Holder, David Hernández-Uribe, James Worthington
Visualization: Jordan W. Wang
Writing – original draft: Jordan W. Wang
Writing – review & editing: Jordan W. Wang, Paul Kapp, Robert Holder, John He, David Hernández-Uribe, James Worthington

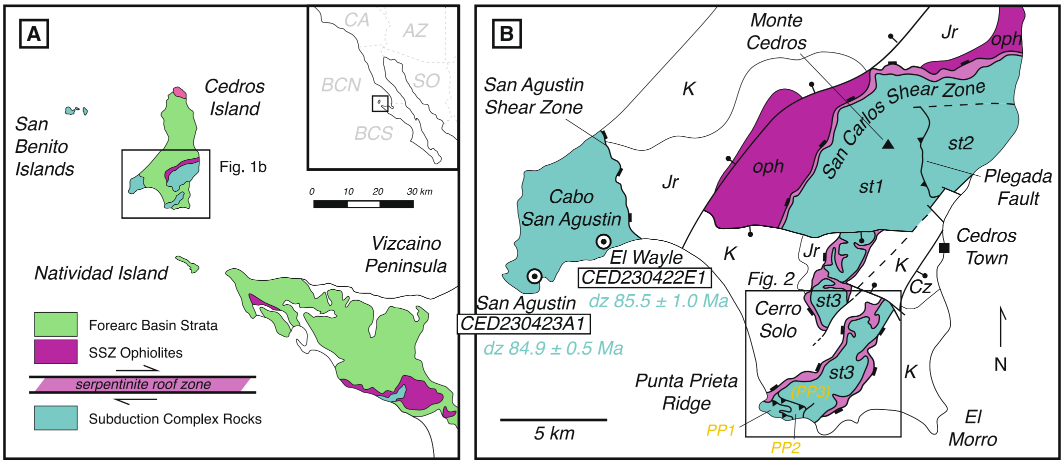

C Subterrane	Distinguishing Characteristics	Temperature (°C)	Pressure (GPa)
st1	Mostly metabasite, strongly foliated, schistose blueschists	250 – 350	0.8 – 1.1
st2	Mostly turbidites, moderate foliation/deformation	170 – 220	0.7 – 0.8
st3	Mostly metabasite and chert, weakly foliated/deformed	180 – 200	0.5 – 0.6

Figure 1. Maps showing regional geologic context. (a) Geologic sketch map of Cedros-Vizcaíno region highlighting main structural-stratigraphic elements. Upper plate basement is composed of Late Triassic and Middle Jurassic suprasubduction zone ophiolites and intruding arc rocks (pink) and is depositionally overlain by forearc basin strata (mostly Jurassic-Cretaceous). High-pressure/low-temperature subduction complex rocks of the lower plate are exposed below the forearc upper plate and exhumed along serpentinite matrix mélange shear zones. Mapping after Sedlock (1988a) and Kimbrough and Moore (2003). (b) Geologic sketch map of southern Cedros Island after Sedlock (1988a) highlighting major fault zones and exposure of lower plate subduction complex rocks, serpentinite roof zone, and upper-plate ophiolites. Approximate location and maximum depositional age of detrital zircon samples from Cabo San Agustin marked by white circles with black dots and name of nearby fishing field. New map units are labeled in yellow. Note: PP3 is equivalent to Sedlock's st3. Forearc basin strata not colored, but major depositional contacts between Jurassic (Jr), Cretaceous (K), and Cenozoic (Cz) strata are drawn to show age relationships across fault boundaries. (c) Key explaining lithologic, structural, and thermobarometric classification of subterranes after Sedlock (1988a).

metasedimentary-rich rocks accreted after ca. 125 Ma, but the first ~50 Myr of the documented subduction history from ca. 180 to 130 Ma are recorded exclusively in high-grade blocks in mélange that constitute <<1% of the volume of accreted material (Wakabayashi, 2015). These older blocks and small slabs are now dispersed over hundreds of localities in the Coast Range but exhibit structural and petrologic evidence for original accretion as coherent fault-bounded nappes composed mostly of metamafic rocks at >10 kbar crustal depths (Dumitru et al., 2010; Wakabayashi, 2017). There is significant debate over how these blocks were exhumed and incorporated into lower-grade metasedimentary- and serpentinite-matrix mélanges, with some workers favoring a purely tectonic mixing mechanism, such as corner flow (Cloos, 1982; Harvey et al., 2021), and others favoring a sedimentary origin, where the high-pressure rocks were originally accreted as thrust nappes, exhumed to the surface via extension and/or erosion, and later incorporated as olistoliths into their mélange host matrix via sedimentary processes before being re-deformed along plate interface shear zones (Malavieille et al., 2016; Wakabayashi et al., 2011). The former view suggests that high-pressure metamorphic blocks of the Franciscan represent stochastic sampling of the subduction interface i.e. mainly limited by material constraints (i.e., the presence of a large amount of low-viscosity material to form the subduction channel), whereas the latter view suggests that high-pressure rocks may have been preferentially exhumed in response to evolving wedge dynamics driven by changes in sediment supply to the trench, coastal erosion rates, coupling of the plate interface, and plate kinematics.

In this paper, we present new geologic mapping, structural observations, and geochronology for well-exposed subduction complex rocks in the Cedros-Vizcaíno region of west central Baja California, Mexico (Figure 1). These rocks are along-strike correlatives to the Franciscan Complex of California, representing Mesozoic remnants of a Panthalassic oceanic plate (probably the Farallon plate) that were subducted and accreted to North America along a long-lived east-dipping subduction zone (Boschman et al., 2018; Busby, 2004; Busby & Centeno-García, 2022). With new field and analytical data, we discuss their history of structural assembly,

19449194, 2026, 4, Downloaded from https://agupubs.onlinelibrary.wiley.com/doi/10.1029/2025TC009340, Wiley Online Library on [01/06/2026]. See the Terms and Conditions (https://onlinelibrary.wiley.com/terms-and-conditions) on Wiley Online Library for rules of use; OA articles are governed by the applicable Creative Commons License

19449194, 2026, 4, Downloaded from https://agupubs.onlinelibrary.wiley.com/doi/10.1029/2025TC009340, Wiley Online Library on [01/06/2026]. See the Terms and Conditions (https://onlinelibrary.wiley.com/terms-and-conditions) on Wiley Online Library for rules of use; OA articles are governed by the applicable Creative Commons License

metamorphism, deformation, and exhumation to the surface and propose a multi-cyclical model where rocks are accreted as coherent nappes at the base of the forearc wedge, exhumed and attenuated along extensional shear zones during phases of supercritical taper, and eventually eroded and recycled back into the subduction trench. We conclude by exploring correlations with the Franciscan and other coeval subduction complexes along the western North American cordilleran margin and speculate on broader implications for subduction dynamics.

2. Regional Geology

Forearc rocks of the Cedros Island-Vizcaíno Peninsula region preserve a discontinuous record of east-dipping subduction from Late Triassic to Late Cretaceous time and the transition from a strongly extensional to strongly contractional convergent margin during the mid-Cretaceous (Figure 1; Boschman et al., 2018; Busby, 2004). The rocks can be broadly divided into two groups based on metamorphic grade and structural superposition: (a) low-grade arc/ophiolite sequences and depositionally overlying arc basin strata of the upper plate; and (b) blueschist-bearing subduction complex rocks of the lower plate (Sedlock, 1988c). Upper and lower plate rocks are separated from one another along a variably attenuated zone of serpentinite-matrix mélange that contains exotic blocks of greenschist, blueschist, amphibolite, and eclogite (Baldwin & Harrison, 1992; Kimbrough & Moore, 2003; Sedlock, 1988b).

The upper-plate forearc basin is composed of deep marine arc- and continental-derived turbiditic strata depositionally overlying polygenetic arc/ophiolite basement. The ophiolitic substrate includes the ca. 221 Ma Vizcaíno ophiolite and the ca. 173 to 164 Ma Cedros Island ophiolite complex, both of which exhibit suprasubduction zone (SSZ) geochemical signatures, are intruded by Late Jurassic to Early Cretaceous plutons, and are deformed by extensional structures (Kimbrough & Moore, 2003; Sedlock, 2003). The overlying forearc basin strata are regionally heterogenous but are generally dominated by Upper Jurassic to Lower Cretaceous deep marine turbidite-bearing strata, volcaniclastic gravity density flows, slump facies, and olistostromes. All rocks of the forearc upper plate are dissected by high- and low-angle normal faults which locally exhume blueschist-bearing subduction zone assemblages of the lower plate in their footwalls (Busby, 2004; Sedlock, 1996; Smith & Busby, 1993).

Subduction-complex rocks of the lower plate are locally (m- to 100-m scale) heterogeneous and chaotically deformed but exhibit regional structural organization in the form of km-scale low-angle nappes characterized by distinct pressure-temperature conditions, lithology, degree, and style of strain, and fault boundaries (Kimbrough, 1985; Rangin, 1979; Sedlock, 1988b). On Cedros Island, subduction complex rocks are superbly exposed in three local uplifts at (a) Monte Cedros and Cerro Solo, (b) the San Agustin promontory, and (c) Punta Prieta Ridge (Figure 1b). Previous work by Sedlock (1988b) interpreted oceanic rocks in these areas as imbricates of penetratively deformed but coherent ocean plate stratigraphy with lesser amounts of mélange metamorphosed to temperatures ~170°C–350°C and pressures from ~5 to >8 kbar. High-pressure blocks from serpentinite- and metasedimentary-matrix mélange constitute a volumetrically minor but chronologically significant record of subduction metamorphism, yielding hornblende (from garnet amphibolite) and white mica (from blueschist) $^{40}Ar/^{39}Ar$ cooling ages of 173 to 165 and 113 to 95 Ma, respectively (Baldwin & Harrison, 1992). Gonzalez and Baldwin (2019) conducted multi-domain diffusion modeling of white mica on some of the same exotic block samples. They demonstrated that an older amphibolite block records slow-cooling and exhumation (~0.04 kbar/Myr) from ca. 180 to 145 Ma whereas two younger blueschist blocks record rapid exhumation (~2 kbar/Myr) from ca. 120 to 115 Ma. However, no geochronological constraints exist for the coherent units described by Sedlock (1988b), and the field contexts for dated blocks are not well constrained.

In the following sections, we focus on the geology of Punta Prieta Ridge (Figure 2) and geochronology of high-pressure blocks and their matrix to constrain the age of subduction accretion and metamorphism and the mechanisms of high-pressure rock exhumation.

3. Structural Geology of Punta Prieta Ridge

We present structural mapping, measurements, field observations, and kinematic interpretations of subduction complex rocks exposed in the core of Punta Prieta Ridge, an ~7.5 km-long and ~1–2 km-wide NE-SW-trending range located on the southeast corner of Cedros island (Figure 2). Previous workers showed that metamorphosed subduction complex rocks are exhumed in the footwalls of range-bounding normal faults that carry non-metamorphosed deep marine forearc basin strata of the Cretaceous Valle Group in their hangingwalls

10.1029/2025TC009340

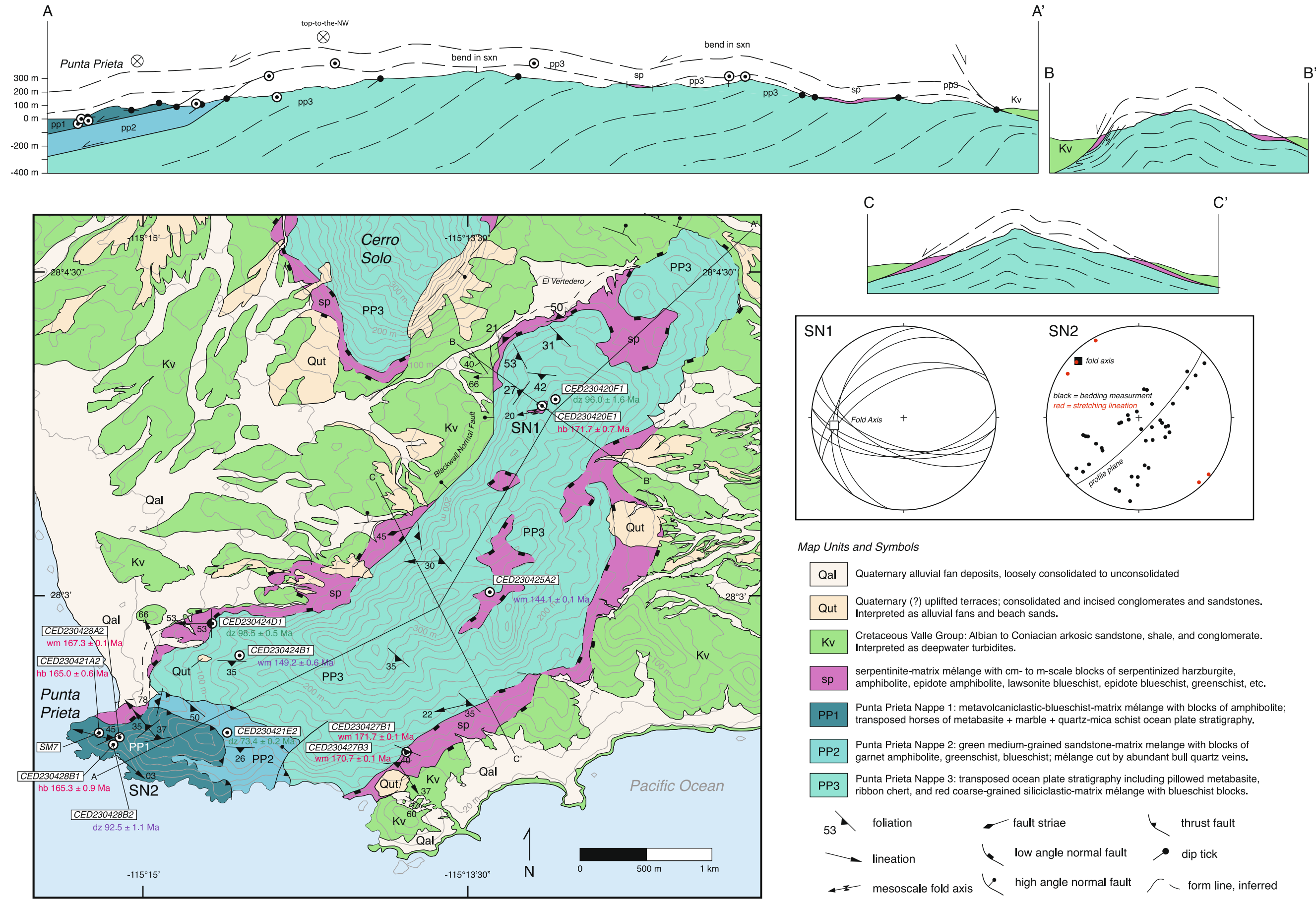

Figure 2. Geologic map of Punta Prieta Ridge, Cedros Island, Baja California. Interpreted ages for each sample are listed next to sample names: dz = detrital zircon maximum depositional age, hb = hornblende ^{40}Ar/^{39}Ar cooling age, wm = white mica ^{40}Ar/^{39}Ar cooling age. Colored text for age data indicates metamorphic grade of dated material; red = amphibolite-facies, blue = blueschist-facies, green = lawsonite-albite facies. All age data are from this study. Stereonet SN1 is a beta diagram showing the orientation of scaly cleavage in serpentinite (great circles) that define open west-plunging folds developed in the northern klippe of the serpentinite roof zone depicted in Figures 3e and 3f. Stereonet SN2 is a pi diagram depicting poles to foliation measurements (black dots) and stretching lineations (red dots) made in blue-green (sodic-calcic) amphibole schists of PP1. Approximate areas where structural data was collected marked on map as SN1 and SN2.

(Kimbrough, 1985; Sedlock, 1988c). Hanging-wall strata dip moderately to shallowly to the southwest and northwest and are cut by pervasive small-displacement high-angle brittle normal faults (Sedlock, 1996; Smith & Busby, 1993). Subduction complex rocks of the footwall range from prehnite-pumpellyite to lawsonite-albite-facies and are strongly disrupted but in some localities retain original ocean plate stratal continuity at the outcrop scale (Sedlock & Isozaki, 1990) and are organized at a mappable scale in tabular nappes with internal foliations and bounding faults that dip southwest (Rangin, 1978; Sedlock, 1988a). We build upon the reconnaissance mapping of Sedlock (1988a), who showed that coherent and disrupted subduction complex rocks of the ridge core are exposed below a variably attenuated zone of penetratively deformed serpentinite-matrix mélange with a high density (>80% in places) of exotic blocks. We refine the extent of his serpentinite-matrix mélange unit in our mapping and recognize three distinct subunits of structurally lower subduction-complex rocks within the core of the range, defined by distinct metamorphic grade, degree of strain, and mapped bounding faults/shear zones. We describe the geometry and lithology of the mapped units and intervening faults from structurally highest to lowest and provide brief kinematic interpretations in concurrent subsections.

3.1. Range Bounding Extensional Structures and Serpentinite Roof Zone

3.1.1. Geometry and Field Observations

At the range front, the Cretaceous Valle Group [Kv] is juxtaposed against structurally underlying ultramafic rocks [sp] exhumed in the footwall of a multiply folded, domal moderate- to low-angle normal fault (Figures 3a and 3b).

19449194, 2026, 4, Downloaded from https://agupubs.onlinelibrary.wiley.com/doi/10.1029/2025TC009340, Wiley Online Library on [01/06/2026]. See the Terms and Conditions (https://onlinelibrary.wiley.com/terms-and-conditions) on Wiley Online Library for rules of use; OA articles are governed by the applicable Creative Commons License

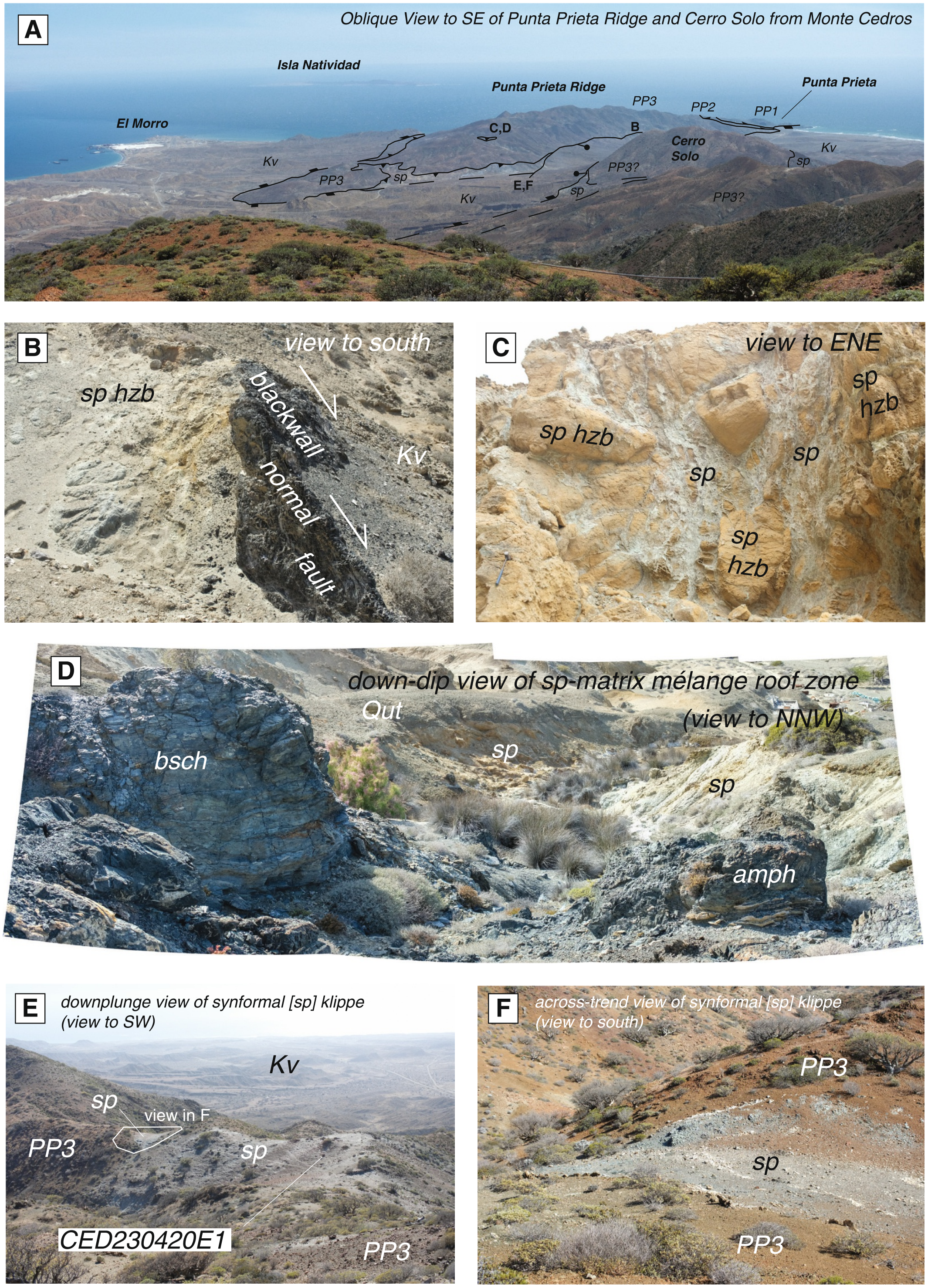

Figure 3. Annotated field photos of Punta Prieta Ridge and the serpentinite roof zone. (a) Oblique view to the southeast of mapped area around Punta Prieta Ridge and Cerro Solo taken from Monte Cedros. Unit abbreviations and structural symbology as in Figure 2. Approximate location of other photos marked for reference. (b) Range-bounding high-angle normal fault separating Cretaceous turbidites of the Valle Group in the hangingwall from serpentinized harzburgite of the serpentinite roof zone in the footwall. (c) View of serpentinized harzburgite blocks in serpentinite-matrix characteristic of upper levels of the serpentinite roof zone. (d) Down-dip view of the serpentinite roof zone showing transition from mostly serpentinized harzburgite at higher structural levels to high-density block-in-matrix mélange with high-pressure blocks at lower structural levels. (e) Down-plunge view of synformal serpentinite roof zone klippe at the northern end of the range. (f) Zoomed-in across-trend view of mesoscale synform in (e).

19449194, 2026, 4, Downloaded from https://agupubs.onlinelibrary.wiley.com/doi/10.1029/2025TC009340, Wiley Online Library on [01/06/2026]. See the Terms and Conditions (https://onlinelibrary.wiley.com/terms-and-conditions) on Wiley Online Library for rules of use; OA articles are governed by the applicable Creative Commons License

19449194, 2026, 4, Downloaded from https://agupubs.onlinelibrary.wiley.com/doi/10.1029/2025TC009340, Wiley Online Library on [01/06/2026]. See the Terms and Conditions (https://onlinelibrary.wiley.com/terms-and-conditions) on Wiley Online Library for rules of use; OA articles are governed by the applicable Creative Commons License

The composition and structure of the ultramafic rocks change over ∼10–20 m structurally below the normal fault from meter-scale kernel-textured serpentinized harzburgite, to a serpentinite-matrix mélange with only m-scale harzburgite blocks (Figures 3b–3d), to a serpentinite-matrix (locally chorite-actinolite) mélange in which >80% of the m-scale blocks are exotic (i.e., not harzburgite and varying in metamorphic grade; Figure 3d). The harzburgite-block mélange varies in thickness (m to 10-m scale) and appears to be equivalent to the overlying kernel-textured harzburgite, albeit with greater degree of serpentinization and higher-strain. The exotic-block mélange is variably attenuated (ranges between 1- and 10-m thickness) and contains blocks of garnet-amphibolite, epidote-amphibolite, lawsonite-blueschist, epidote-blueschist, and greenschist. Henceforth, we refer to this structurally high package of ultramafic rocks and its regional correlatives as the "serpentinite roof zone." This zone is mesoscopically folded but generally follows the topographic contours of the range and is exposed in synformal klippen near topographic highs (Figures 3e and 3f). The preservation of these klippen suggest that the local structural relief is on the order of several hundred meters and probably <1 km. Foliation dip, stretching lineations, and mesoscale fold axes in the mélange are generally oriented from WNW to ESE (Figure 2).

Immediately below the serpentinite roof zone, subduction complex rocks are strongly foliated and lineated parallel to fabrics in the overlying mélange zone (WNW to ESE) ∼100–150-m down into the lower plate. Deformation fabrics in this zone are defined by brittle fault breccias and Riedel shears developed in sodic-calcic amphibole-schists (Figure 4a), ductile stretching lineations and stretched pebbles (Figure 4b), layer/foliation-parallel boudinage (Figure 4c), and constrictional folds in weaker low-grade metasedimentary protoliths (Figure 4d). The strong WNW-ESE fabric overprints recumbent folds developed in metasedimentary rocks, creating complex fold interference patterns indicative of constrictional strain and/or structural re-orientation of older fabrics (Figures 4d and 5b–5d; e.g., Fossen et al., 2013). On the northwest side of the range, a high-angle curviplanar normal fault ("Blackwall Normal Fault" on Figure 2) locally cuts out the serpentinite unit and the range-bounding low-angle normal fault (Figure 2).

3.1.2. Kinematic Interpretations

Following previous workers, we interpret the most recent phase of deformation in the serpentinite-matrix mélange zone and associated structures as being dominated by extensional strain that accommodated the attenuation of the upper-plate mantle (structurally high serpentinized harzburgite) and exhumation of underlying subduction complex rocks (exotic-block serpentinite-matrix mélange and structurally underlying nappes) (Kimbrough, 1985; Sedlock, 1996; Smith & Busby, 1993). Our mapping, structural measurements, and observation of brittle-ductile fabrics developed within the underlying subduction complex suggest that extensional strain included significant components of pure shear and was transmitted ∼100–150 m into the subduction complex footwall of the range-bounding normal faults, producing open folds with WNW-ESE-trending fold axes parallel to stretching lineations and reorienting older asymmetric and recumbent folds developed in weak metasedimentary protoliths (Figures 5b–5d). Based on cross-cutting relationships with uplifted marine terrace deposits and Quaternary alluvial fans, we interpret the Blackwall normal fault and the conjugate fault bounding the southeast side of Cerro Solo to be Neogene-Quaternary structures responsible for the modern topographic relief.

3.2. Internal Architecture of Punta Prieta Ridge Subduction Complex

3.2.1. Geometry and Field Observations

Below the serpentinite-matrix mélange roof zone, subduction complex rocks are organized in tabular fault-bounded units distinguished by lithology, metamorphic grade, and degree of strain. The structurally highest unit [PP1] crops out near the southwest end of the ridge at Punta Prieta ("Dark Point") and is the namesake of the point and ridge. It is composed of a diverse assemblage of moderately- to strongly-foliated fine- to medium-grained high-P/T lithologies including blue-green (sodic-calcic) amphibole-quartz-white mica-epidote schists, calc-schists, metachert, and minor serpentinite, which was documented in shear zones separating faults slices of siliciclastic rocks in an outcrop-scale duplex (Figure 5).

Meter-scale garnet- and epidote-bearing amphibolite blocks are abundant within the lower-grade siliciclastic lithologies of PP1 and crop out individually as well as together in clusters within outcrop-scale pods of chlorite-actinolite-serpentinite matrix (Figure 6a). Locally, the relationship between these blocks and the dominant PP1 lithology is demonstrably sedimentary, with higher-grade blocks completely surrounded by lower-grade, lower-

10.1029/2025TC009340

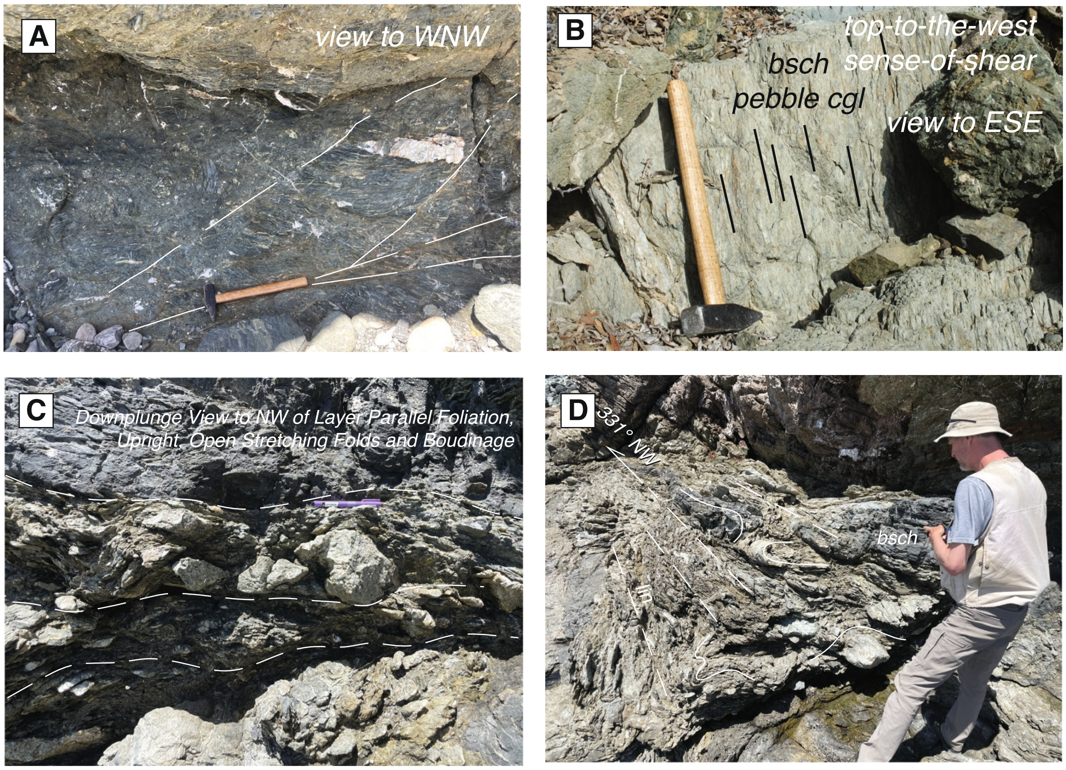

Figure 4. Annotated outcrop photos of brittle-ductile extensional structures developed immediately below the serpentinite roof zone. (a) Brittle fault breccia and Riedel shears developed in sodic-calcic amphibole-quartz-mica-schist of PP1. Hammer is ~40 cm-long for scale. (b) Stretch blueschist-pebble conglomerate of PP3 from immediately below the serpentinite roof zone near Figure 3d. (c) Down-plunge view of layer parallel boudinage and upright open folds developed in siliciclastic rocks of PP1. Pen is ~14 cm-long for scale. (d) Oblique view of the same outcrop as in C showing strongly developed stretching lineation, fold interference patterns, and large blueschist block in siliciclastic matrix. Kapp for scale is pointing in the direction of stretching, trending ~331° NW.

strain metaclastic rock. Well-foliated siliciclastic rocks of PP1 are cut by pervasive quartz and carbonate veins, which are themselves folded and deformed, suggesting that large volume dissolution-precipitation occurred over multiple phases of deformation.

The base of PP1 is a discrete low-angle fault contact that dips southwest (Figures 2 and 6b) and places higher-grade sodic-calcic amphibole-schists over lower-grade metasedimentary rocks of unit [PP2]. PP2 is predominantly composed of green micaceous shale- and fine- to medium-grained metasandstone-matrix-mélange with cm- to meter-scale blocks of highly weathered garnet-amphibolite and epidote-blueschist and more tabular meter-scale horizons of serpentinite and metasandstone (Figure 6b). The siliciclastic matrix of PP2 is weakly foliated parallel and adjacent to bounding fault contacts but does not exhibit a well-developed internal shear fabric. Like PP1, metasedimentary rocks of PP2 are cut by pervasive quartz veins, indicative of large volume dissolution-precipitation. PP2 structurally overlies lower-grade red-weathering rocks of nappe PP3 along a moderately southwest dipping shear zone associated with a 1-2 m-thick zone of serpentinite and strongly foliated mudstone of PP3 in the footwall.

PP3 is composed of structurally imbricated and transposed decameter-scale panels of siltstones, fine-grained sandstones (greywackes), and meter-scale horizons of blueschist-bearing stretched pebble conglomerates, interpreted as thin-bedded turbidites based on key exposures where primary sedimentary structures are observed (Sedlock & Isozaki, 1990). These rocks exhibit a strongly developed bedding-parallel cleavage. Also present are 100-m scale exposures of radiolarian ribbon chert and local, isolated occurrences of pillow basalt (Figure 7f). Metamorphic mineral assemblages in these rocks are generally fine-grained and include chlorite, albite, titanite, aragonite, and jadeitic pyroxene, as well as very fine-grained (and rare) lawsonite porphyroblasts (Sedlock, 1988b). Cobble- to boulder-sized higher-grade blocks (predominantly [lawsonite] blueschist, more rarely

19449194, 2026, 4, Downloaded from https://agupubs.onlinelibrary.wiley.com/doi/10.1029/2025TC009340, Wiley Online Library on [01/06/2026]. See the Terms and Conditions (https://onlinelibrary.wiley.com/terms-and-conditions) on Wiley Online Library for rules of use; OA articles are governed by the applicable Creative Commons License

19449194, 2026, 4, Downloaded from https://agupubs.onlinelibrary.wiley.com/doi/10.1029/2025TC009340, Wiley Online Library on [01/06/2026]. See the Terms and Conditions (https://onlinelibrary.wiley.com/terms-and-conditions) on Wiley Online Library for rules of use; OA articles are governed by the applicable Creative Commons License

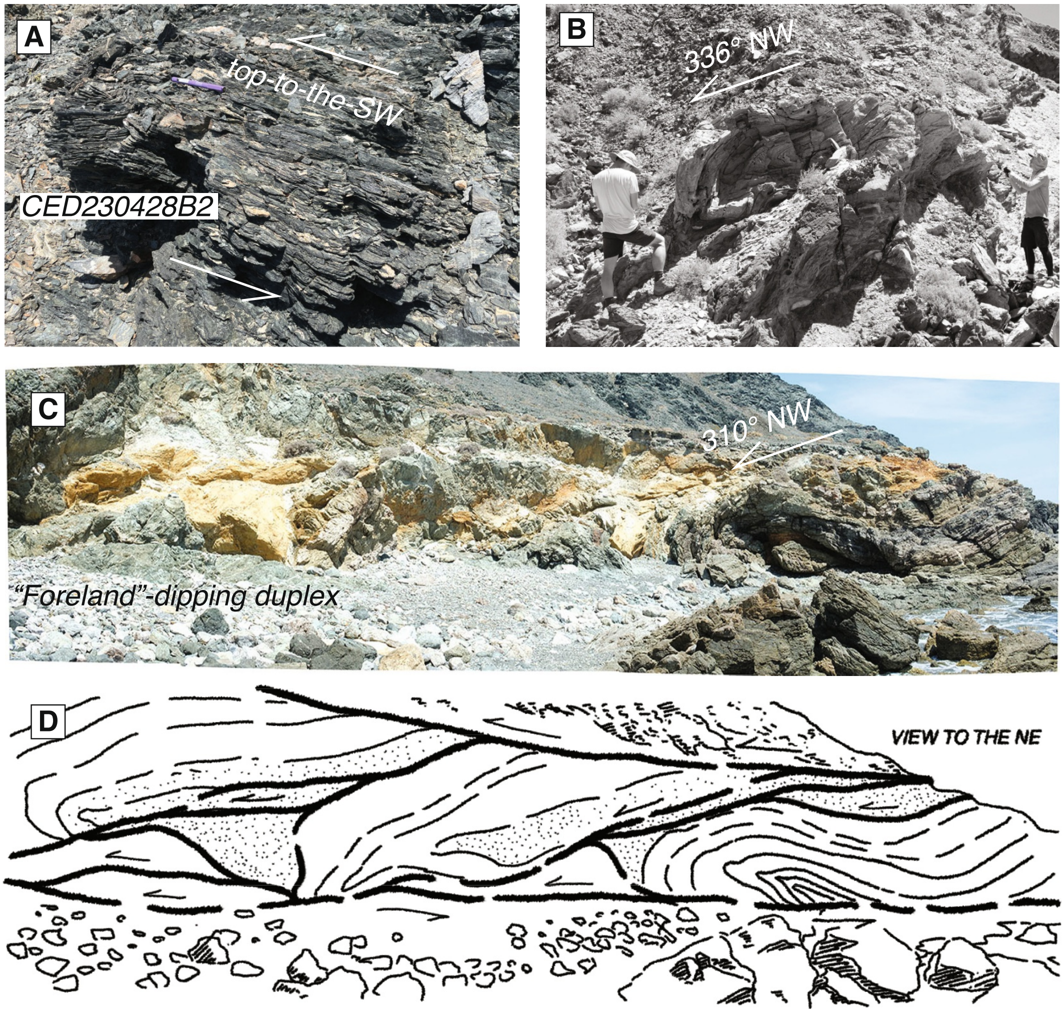

Figure 5. Annotated field photos of early contractional structures in PP1. (a) Down-dip and down-plunge view of strongly foliated and lineated sodic-calcic amphibole-quartz-mica schist. S-C-C' fabrics, sigma and delta clasts of boudinaged quartzite bands, and kink folds indicated top-to-the-southwest motion before top-to-the-northwest stretching and lineation reorientation. Pen is ~14 cm-long for scale. (b) Cross-sectional view of mesoscale recumbent fold developed in calcschists. Folds are constrictional with fold axes parallel to local stretching lineation trending ~336° NW. He (left) and Holder (right) for scale. (c) Panoramic photo showing cross-sectional view of recumbently folded strata forming foreland-dipping duplex developed in siliciclastic and metaultramafic rocks. Original recumbent folds have been stretched into constrictional folds with axes parallel to local stretching direction, trending ~310° NW. (d) Sketch of C to highlight marker beds and structures making up the recumbent folds and duplex. Stippled unit is penetratively deformed serpentinite.

greenschist, and in one instance a weathered gabbro) in this low-grade sedimentary matrix occur in isolation as well as 100-m scale mélange horizons (Figures 2 and 6c). The blueschist blocks are in some places enveloped in pods or have partial rinds of actinolite + chlorite ± serpentinite schist, but at the meso- and macroscale are demonstrably enveloped within low-grade siliciclastic matrix (Figures 6c and 7). Fine-grained metasedimentary rocks of PP3 host large volumes of quartz and carbonate veins indicative of large-volume solution mass transfer.

3.2.2. Kinematic Interpretations

The structurally highest rocks of PP1 are strongly foliated and lineated and exhibit at least two distinct sets of fabrics that indicate (a) early top-to-the-west/southwest simple shear and (b) later top-to-the-northwest/west constrictional strain and pure shear flattening. We interpret the first set of deformation fabrics in PP1 (S-C-C' fabrics, kink-bands, and brittle fault-breccias developed in sodic-calcic amphibole-schists and recumbent folds and outcrop-scale duplexes developed in weaker lithologies; Figure 5) to represent brittle-ductile contraction

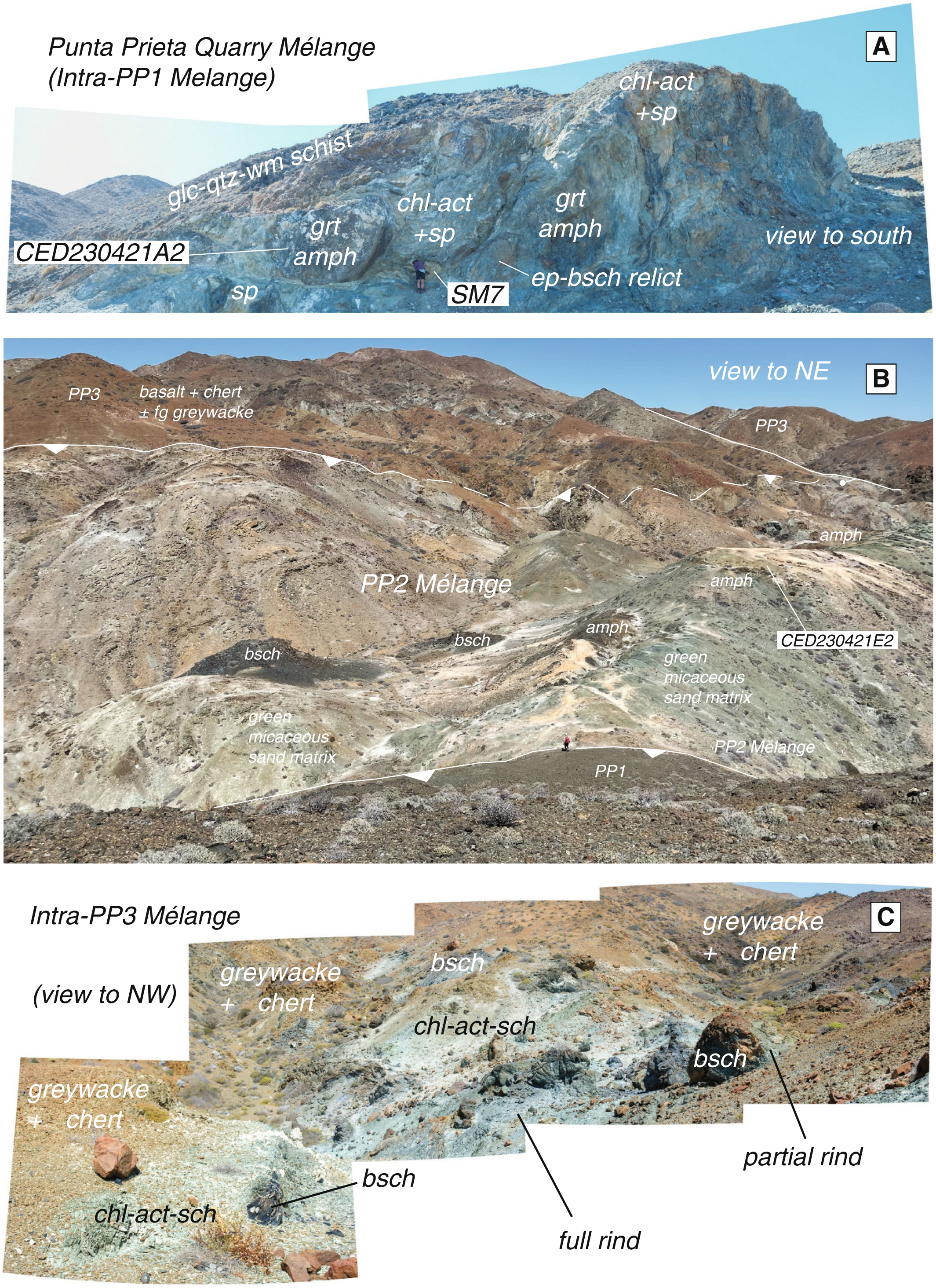

Figure 6. Annotated field photos showing outcrop-scale architecture of mélange horizons in Punta Prieta Ridge subduction complex. (a) Punta Prieta Quarry Mélange showing blocks of garnet-amphibolite, epidote-blueschist, and metasedimentary rocks enveloped within a pod of chlorite-actinolite-serpentinite schist that itself is wrapped within sodic-calcic amphibole-quartz-mica schists of PP1. He in the center bottom of image for scale. (b) View to the NE of PP2 mélange and bounding fault contacts. Most of the pictured material is green micaceous metasandstone matrix, with blocks of blueschist and amphibolite. Holder for scale standing on the thrust fault contact between PP1 and PP2. (c) Blueschist blocks and chlorite-actinolite-schist selvages in transposed fine-grained greywacke and chert of nappe PP3.

19449194, 2026, 4, Downloaded from https://agupubs.onlinelibrary.wiley.com/doi/10.1029/2025TC009340, Wiley Online Library on [01/06/2026]. See the Terms and Conditions (https://onlinelibrary.wiley.com/terms-and-conditions) on Wiley Online Library for rules of use; OA articles are governed by the applicable Creative Commons License

10.1029/2025TC009340

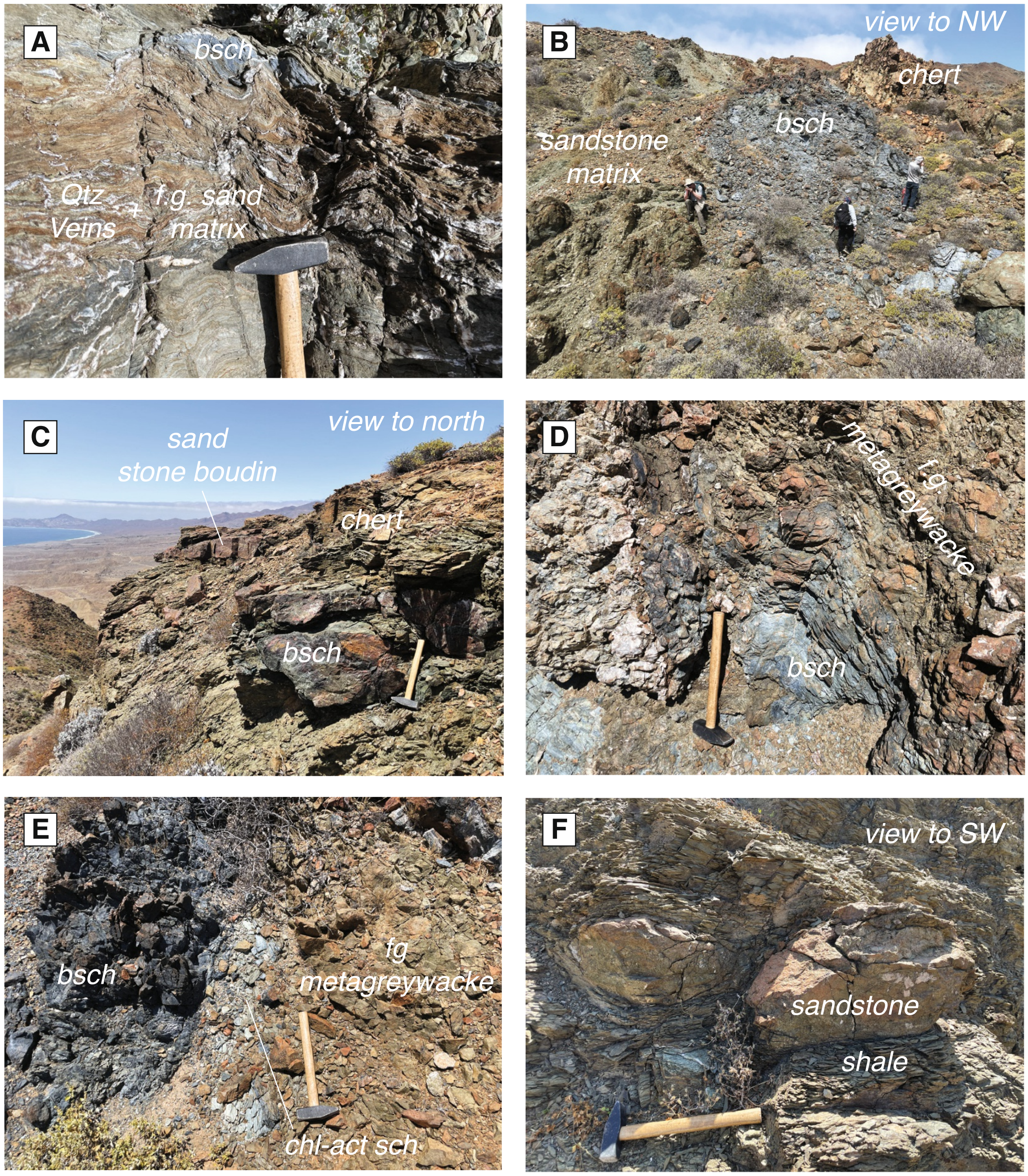

Figure 7. Macroscale observational evidence for sedimentary origin of blueschist material in PP3. (a) Deformed cobble-sized clast of blueschist in fine-grained sandstone matrix of transposed turbidites from PP3. Note extensive layer parallel quartz veining. Head of hammer is ~15 cm-long. (b) Elephant-sized blueschist block enveloped in transposed metasandstone-matrix. From left to right: Kapp, Hernández-Uribe, and Holder for scale. (c) Blueschist boulder in fine-grained coherent turbidites. Handle of hammer is ~40 cm-long. (d) Deformed blueschist boulder in transposed metagreywacke. (e) Blueschist boulder with partial rind of chlorite-actinolite schist enveloped in coherent fine-grained metagreywacke. (f) Sandstone layer boudinaged within scaly shale that includes blueschist pebbles.

along the plate interface during accretion and prograde metamorphism of the unit. We interpret the second set to represent post-accretion constrictional strain, which reoriented earlier fabrics during regional west-northwest-directed extension.

The sedimentary-matrix mélange of PP2 exhibits strong foliations along its fault contacts with overlying PP1 and underlying PP3, but is otherwise relatively weakly deformed, indicating that strain was concentrated along the margins of the unit. Kinematic indicators were not identified in the field, but the bounding faults are interpreted as thrusts based on the relative superposition and metamorphic grade of units (PP1 being the highest grade and PP3 being the lowest).

19449194, 2026, 4, Downloaded from https://agupubs.onlinelibrary.wiley.com/doi/10.1029/2025TC009340, Wiley Online Library on [01/06/2026]. See the Terms and Conditions (https://onlinelibrary.wiley.com/terms-and-conditions) on Wiley Online Library for rules of use; OA articles are governed by the applicable Creative Commons License

Our map unit PP3 is equivalent to rocks of Sedlock's "st3" (Sedlock, 1988c), which he determined to have experienced metamorphic temperatures between 200°C and 180°C and pressures >5–6 kbar based on the presence of lawsonite, aragonite, and composition of jadeitic clinopyroxene (Sedlock, 1988b). Following Sedlock, we interpret PP3 to be an isofacial duplex composed of structurally imbricated oceanic crust. Sedlock and Isozaki (1990) studied a large coherent horse of ocean plate stratigraphy within PP3 that exhibits primary depositional contacts between pelagic chert, underlying metabasites, and overlying thin-bedded siliciclastic turbidites and determined that the ~40 m-thick pelagic section was deposited over >65 Myr from latest Triassic/earliest Jurassic to Early Cretaceous time before entering the trench. These estimates provide primary constraints on the age of the subducting oceanic lithosphere and the P-T conditions during subduction accretion and low-grade metamorphism. In the following section, we present new $^{40}Ar/^{39}Ar$ ages for high-pressure blocks and detrital zircon data from PP1, PP2, and PP3 siliciclastic rocks to provide further constraints on the ages of subduction accretion and metamorphism and the age relationships between blocks and their host matrix.

4. Analytical Methods

4.1. $^{40}Ar/^{39}Ar$ Instrumentation, Analyses, Data Reduction, and Age Interpretation

Homogeneous mineral separates for $^{40}Ar/^{39}Ar$ analysis were prepared by standard methods of crushing, sieving, magnetic separation, and hand-picking under binocular microscope. Each aliquot included 10–35 mg of 250–500 μm white mica, hornblende, or intergrown sodic amphibole + white mica. Sample aliquots were wrapped in aluminum foil, placed in 2.5 cm aluminum disks, and irradiated in the Cadmium-Line In-Core Irradiation Tube of the Oregen State University TRIGA reactor. Reference material FC-2 (28.201 Ma) was irradiated with sample material to monitor neutron flux.

$^{40}Ar/^{39}Ar$ step heating experiments were conducted at the Arizona Noble Gas Laboratory at the University of Arizona. Sample aliquots were placed in 5 mm wells within a copper planchette and incrementally heated by a Teledyne Instruments 55 W CO_2 laser. Extracted gas was purified for 20–30 min using a custom extraction line including two hot (450°C) getters, one room temperature getter, and a cold finger maintained at −90°C. After cleaning, gas was analyzed using a Thermo Fisher Scientific Argus VI multicollector noble gas mass spectrometer.

Data were reduced and plotted using the PyChron software of Ross (2017). J-values range from 1.324E−05 to 1.336E05 and are reported for each sample in Supporting Information S1. $^{40}Ar/^{39}Ar$ dates were calculated using decay constants from Min et al. (2000) and an atmospheric $^{40}Ar/^{36}Ar$ ratio of 298.56 ± 0.31 from Lee et al. (2006). Inverse isochron plots were used to verify the trapped component of $^{40}Ar/^{36}Ar$ is close to atmospheric and are included in Supporting Information S1.

When possible, we report the plateau date of experiments. Plateaus were automatically determined in PyChron for experiments with five or more contiguous steps that comprised >50% of released ^{39}Ar and did not have a slope (no ascending or descending steps), and where isochrons regressed through the plateau steps yielded initial $^{40}Ar/^{36}Ar$ values within a 95% confidence interval of the atmospheric value (Schaen et al., 2021). When plateaus are not present, we report the integrated age.

4.2. Detrital Zircon U-Pb LA-ICP-MS Methodology

Detrital zircons were separated from metasedimentary samples using standard methods of crushing, sieving, water separation, magnetic separation, and heavy liquids. After separation, zircons were poured on tape and mounted with primary reference material FC-1 and secondary reference materials R33 and SL-F in epoxy. Epoxied mounts were polished to maximize exposed surface area of grains. Back-scattered electron and cathodoluminescence (CL) images were acquired on a Hitachi 3400 scanning electron microscope to provide chemical and textural context for laser spot placement.

Detrital zircon analysis by LA-ICP-MS was conducted at the Arizona Laserchron Center following the methods of Gehrels et al. (2008), Gehrels and Pecha (2014), and Pullen et al. (2018). Prior to analysis, a 40 μm cleaning shot was used to remove any contaminants or common lead on the surface of the grain mount. Samples were then ablated using a 15 μm spot size with a Teledyne Iridia 193 nm excimer laser. Ablated material was carried through an aerosol rapid introduction system to the ion source of a ThermoScientific Element2 high-resolution single-collector ICP-MS, where relevant ions of U, Th, Pb, and Hg were analyzed via peakhopping. Analyses were run

19449194, 2026, 4, Downloaded from https://agupubs.onlinelibrary.wiley.com/doi/10.1029/2025TC009340, Wiley Online Library on [01/06/2026]. See the Terms and Conditions (https://onlinelibrary.wiley.com/terms-and-conditions) on Wiley Online Library for rules of use; OA articles are governed by the applicable Creative Commons License

19449194, 2026, 4, Downloaded from https://agupubs.onlinelibrary.wiley.com/doi/10.1029/2025TC009340, Wiley Online Library on [01/06/2026]. See the Terms and Conditions (https://onlinelibrary.wiley.com/terms-and-conditions) on Wiley Online Library for rules of use; OA articles are governed by the applicable Creative Commons License

using sample-standard bracketing with primary reference material FC-1 (ID-TIMS age of 1,099.0 ± 0.6 Ma; Paces & Miller, 1993) to monitor and correct for instrument drift during the analysis session.

Data were reduced and processed using the *MatLab* program *AgeCalcML_E2* (Sundell et al., 2021). Detrital zircon age spectra and plots were generated using the programs *detritalPy* and *isoplotR* (Sharman et al., 2018; Vermeesch, 2018). Weighted mean $^{206}Pb/^{238}U$ results for secondary reference materials R33 and SL-F were calculated for each analysis session and were found to be within uncertainty of their respective reference ages (ID-TIMS ages of 419.3 ± 0.4 and 555.86 ± 0.68 Ma, respectively; see Wang et al., 2022 and references therein). For each sample, we calculate maximum depositional ages (MDAs) using the maximum likelihood age (MLA) method of Vermeesch (2021) and the youngest statistical population (YSP) method of Coutts et al. (2019).

5. Results

5.1. Block Descriptions and $^{40}Ar/^{39}Ar$ Results

Below, we describe the structural and petrologic context for eight high-pressure blocks-in-mélange sampled across Punta Prieta Ridge from structurally highest to lowest and report the results of $^{40}Ar/^{39}Ar$ step-heating analyses (Figure 8). After determining the age of a sample, we provide brief interpretations on the geologic significance of the age based on the metamorphic grade of the sample and the nominal closure temperatures of the mineral(s) analyzed. Summaries of sample locations, lithology, and geochronologic results are provided in Table 1.

5.1.1. Sample CED230420E1

Sample CED230420E1 is a small (<10 cm) block of garnet-hornblende gneiss with titanite and apatite as well as minor epidote, rutile, and quartz. It was collected from a synformal serpentinite-matrix mélange klippe structurally overlying PP3 near the northeast end of the ridge (Figures 2, 3e, and 8a). Amphiboles from the matrix of the sample exhibit textural zoning and amphibole inclusions in garnet cores exhibit blue-green pleochroism different from the matrix, suggesting preservation of multiple metamorphic parageneses. An aliquot of hornblende (mean grain size ∼250–350 μm) yields an apparent age spectra with an initial rise in the first 5% of cumulative $\%^{39}Ar$ from ca. 140 Ma to a plateau of ca. 171 Ma and a sharp decrease back to ca. 140 Ma in the last 10% of cumulative $\%^{39}Ar$. K/Ca ratios in the first 5% are initially high but decrease and plateau with the ca. 171 Ma age steps before decreasing slightly in the last 10% of the experiment. We interpret the plateau age of 171.7 ± 0.7 Ma (mean square weighted deviation [MSWD] = 1.2, $n = 9$, $\%^{39}Ar = 80\%$) to represent the minimum cooling age for hornblende through the nominal Ar-closure window.

5.1.2. Sample CED230427B1

Sample CED230427B1 was collected from a <1 m boulder-sized block of garnet-white mica-chlorite-clinozoisite-plagioclase-quartz-calcic amphibole schist, with minor sodic amphibole, titanite, and apatite, in serpentinite-matrix mélange that structurally overlies PP3 and bounds the southeastern side of Punta Prieta Ridge (Figures 2 and 8b). An aliquot of white mica (mean grain size ∼250–450 μm) yields initial rising age spectra in the first 5% of cumulative $\%^{39}Ar$ released from ca. 152 Ma to a plateau of ca. 172 Ma. We interpret the plateau age of 171.7 ± 0.1 Ma (MSWD = 1.5, $n = 11$, $\%^{39}Ar = 55$) to represent the minimum cooling age for white mica through the nominal Ar-closure window.

5.1.3. Sample CED230427B3

Sample CED230427B3 was collected from 1 to 2 m-sized block of similar lithology to CED230427B1, sampled at the same locality (Figures 2 and 8c). It differs from CED230427B3 in that it is coarser-grained and contains a greater proportion of sodic amphibole. An aliquot of white mica (mean grain size ∼250–400 μm) yields a complicated age spectra with a short initial rise in ages over the first 7% of cumulative $\%^{39}Ar$ released from ca. 167 to 170 Ma while the final 93% of argon released yield steps with ages that oscillate between 173 and 170 Ma. Because of the low-spread in ages throughout the experiment and the similarity with white mica analyzed from adjacent sample CED230427B1, we interpret the integrated age of 170.7 ± 0.1 Ma to represent the minimum cooling age for white mica through the nominal Ar-closure window.

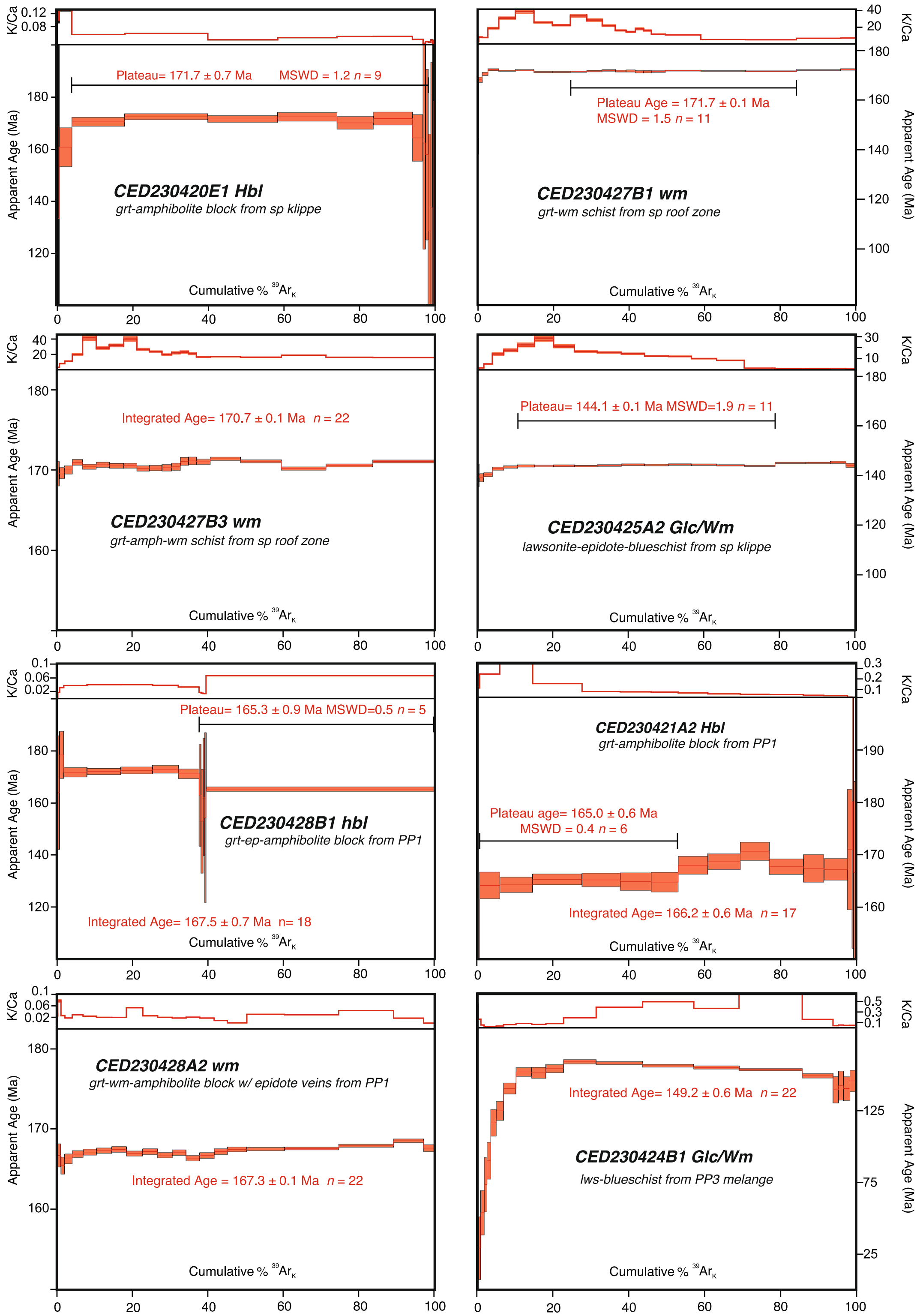

Figure 8. $^{40}Ar/^{39}Ar$ age spectra and K/Ca diagrams from step heating experiments. All errors are reported at 2 sigma.

5.1.4. Sample CED230425A2

Sample CED230425A2 is from a 2 to 3 m-scale block of coarse-grained glaucophane-white mica-chlorite-epidote schist that is enveloped in a chlorite-actinolite schist matrix. We interpret the block to be part of the serpentinite

19449194, 2026, 4, Downloaded from https://agupubs.onlinelibrary.wiley.com/doi/10.1029/2025TC009340, Wiley Online Library on [01/06/2026]. See the Terms and Conditions (https://onlinelibrary.wiley.com/terms-and-conditions) on Wiley Online Library for rules of use; OA articles are governed by the applicable Creative Commons License

10.1029/2025TC009340

Table 1
Summary of Geochronologic Samples

Sample	Description	Lat	Lon	Unit	Method	Mineral	Age	Error (2 sigma)	Notes
$^{40}Ar/^{39}Ar$ samples									
CED230420E1	Garnet-amphibolite block from serpentinite matrix melange klippe	28.064762	−115.21953	sp	$^{40}Ar/^{39}Ar$	Amphibole	171.7	0.7	Plateau age
CED230427B1	Garnet-epidote-white mica-sodic amphibole schist block from serpentinite-matrix melange zone along southeast flank of Punta Prieta Ridge	28.037804	−115.22971	sp	$^{40}Ar/^{39}Ar$	White mica	171.7	0.1	Plateau age
CED230427B3	Garnet-sodic amphibole-white mica-schist block from serpentinite-matrix melange zone along southeast flank of Punta Prieta Ridge	28.037804	−115.22971	sp	$^{40}Ar/^{39}Ar$	White mica	170.7	0.1	Integrated age
CED230425A2	Coarse-grained lawsonite-epidote-blueschist block from serpentinite klippe (?) In middle of range	28.050043	−115.22274	sp?	$^{40}Ar/^{39}Ar$	glc/white mica	144.1	0.1	Plateau age
CED230428B1	Coarse-grained garnet-epidote amphibolite block within PP1 qtz-glaucophane-schist matrix	28.03833	−115.25223	PP1	$^{40}Ar/^{39}Ar$	Amphibole	165.3	0.9	Plateau age
CED230421A2	Coarse-grained garnet-amphibolite block within PP1 qtz-glaucophane-schist matrix	28.039087	−115.25348	PP1	$^{40}Ar/^{39}Ar$	Amphibole	165	0.6	Plateau age
CED230428A2	Coarse-grained garnet-white mica-ampphibolite block within PP1 qtz-glaucophane-schist matrix	28.039037	−115.25176	PP1	$^{40}Ar/^{39}Ar$	White mica	167.3	0.1	Integrated age
CED230424B1	Coarse-grained lawsonite-blueschist block within PP3 siliciclastic-matrix	28.045358	−115.24255	PP3	$^{40}Ar/^{39}Ar$	glc/white mica	149.2	0.6	Integrated age
Detrital Zircon U-Pb samples									
CED230428B2	Fine-grained, well-foliated qtz-glaucophane-schist matrix of PP1	28.03833	−115.25223	PP1	U-Pb	Zircon	92.5	1.1	Maximum likelihood age
CED230422E1	Medium-grained lithic-rich lawsonite- and glaucophane-bearing metasandstone	28.097478	−115.32121	West cedros	U-Pb	Zircon	85.5	1	Maximum likelihood age
CED230423A1	Coarse-grained metasandstone	28.08196	−115.34575	West cedros	U-Pb	Zircon	84.9	0.5	Maximum likelihood age
CED230421E2	Medium-grained green micaceous metasandstone	28.039508	−115.2438	PP2	U-Pb	Zircon	70.9	0.4	Maximum likelihood age
CED230420F1	Strongly deformed low-grade sandstone of PP3	28.06479	−115.21872	PP3	U-Pb	Zircon	96	1.6	Maximum likelihood age
CED230424D1	Medium-coase gr. quartz lithic sandstone with stretched pebbles (oriented)	28.047773	−115.24472	PP3	U-Pb	Zircon	98.5	0.5	Maximum likelihood age

19449194, 2026, 4, Downloaded from https://agupubs.onlinelibrary.wiley.com/doi/10.1029/2025TC009340, Wiley Online Library on [01/06/2026]. See the Terms and Conditions (https://onlinelibrary.wiley.com/terms-and-conditions) on Wiley Online Library for rules of use; OA articles are governed by the applicable Creative Commons License

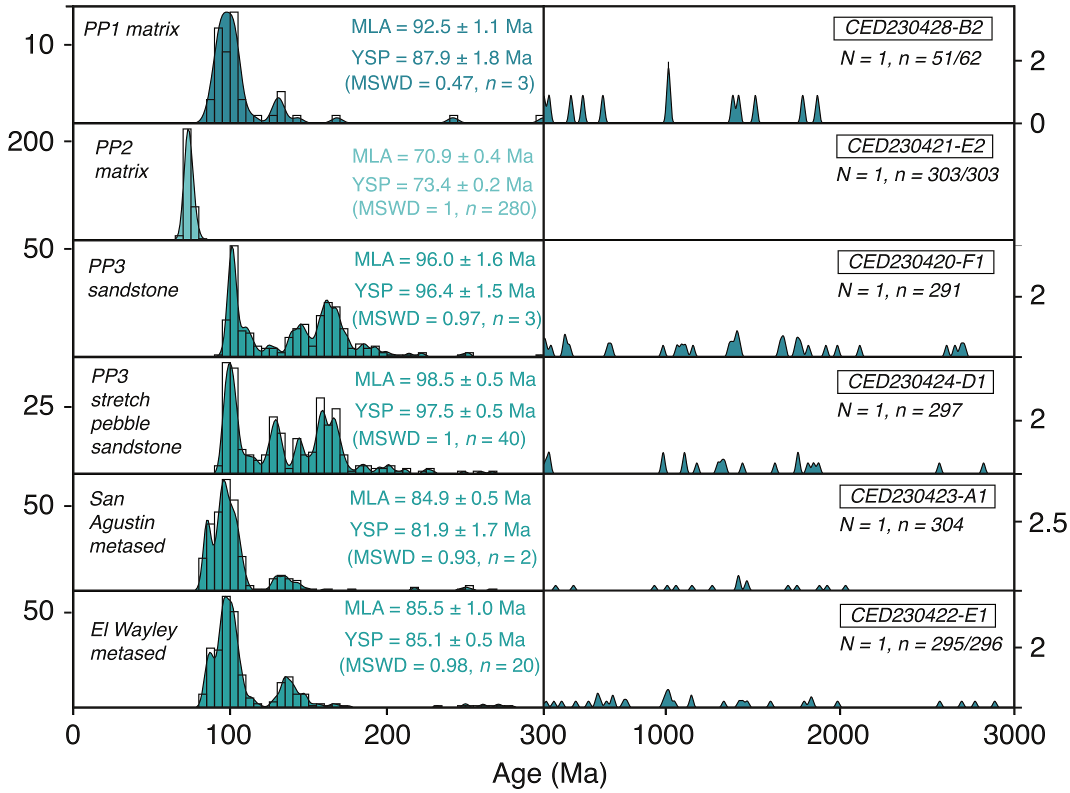

Figure 9. Detrital zircon U-Pb kernel density estimate plots for metasiliciclastic samples from the Cedros subduction complex. Analyses with ages between 300 and 0 Ma are plotted on the left and analyses with ages between 3.5 Ga and 300 Ma to the right. MLA = maximum likelihood age; YSP = youngest statistical population; MSWD = mean square weighted deviation.

roof zone which is exposed as a multiply folded klippe near the topographic high at the center of the range (Figures 2 and 8h). An aliquot of intergrown white mica (mean grain size ~150–200 μm) and glaucophane yields an age spectra with initially rising ages through the first 10% of cumulative $\%^{39}Ar$ released from ca. 140 to 144 Ma. The final 90% of the experiment yielded ages between 144 and 145 Ma with a plateau of 144 Ma defined between 15% and 79% cumulative ^{39}Ar released. We interpret the plateau age of 144.1 ± 0.1 Ma (MSWD = 1.9, n = 11, $\%^{39}Ar$ = 64) to represent the minimum cooling age of white mica through the nominal Ar-closure window, and may approximate the age of peak prograde metamorphism.

5.1.5. Sample CED230428B1

Sample CED230428B1 was collected from one of several meter-scale blocks of garnet-clinozoisite-clinopyroxene-hornblende gneiss above the Punta Prieta Quarry at the southwest end of the ridge (Figures 2 and 8e). The blocks have chlorite-actinolite-serpentine schist rinds All blocks (and their rinds) at this locality are hosted in a well-foliated, fine-grained sodic-calcic amphibole-quartz-white mica schist which we interpret to be a metavolcaniclastic-matrix to the blocks. An aliquot of amphibole (mean grain size ~350–500 μm) yields a complicated age spectrum with an initial pseudo-plateau age of ca. 171 Ma for the first ~40% of cumulative $\%^{39}Ar$ released and a younger plateau age of ca. 165 Ma for the final ~60% of the experiment. We interpret the plateau age of 165.3 ± 0.9 Ma (MSWD = 0.5, n = 5, $\%^{39}Ar$ = 62) as the minimum cooling age for hornblende through the nominal Ar-closure window.

5.1.6. Sample CED230421A2

Sample CED230421A2 was collected from a meter-scale block of very coarse-grained garnet-hornblende-epidote gneiss, with minor rutile, titanite, chlorite, white-mica, and quartz, in-serpentinite-matrix mélange from the Punta Prieta Quarry (Figures 2, 6a, and 8d). Unlike map unit sp, the serpentinite-matrix of the quarry is highly localized

19449194, 2026, 4, Downloaded from https://agupubs.onlinelibrary.wiley.com/doi/10.1029/2025TC009340, Wiley Online Library on [01/06/2026]. See the Terms and Conditions (https://onlinelibrary.wiley.com/terms-and-conditions) on Wiley Online Library for rules of use; OA articles are governed by the applicable Creative Commons License

to regions around amphibolite blocks and appears to be enveloped in well-foliated metaclastic and meta-volcaniclastic rocks of the dominant PP1 lithology. An aliquot of amphibole (mean grain size ~350–450 μm) yields an age spectrum with a young initial first step ca. 158 Ma, a plateau ca. 165 Ma for the first ~50% cumulative $\%^{39}$Ar released, and a more complicated rise and fall into older ages between 172 and 168 Ma for the final half of the experiment. We interpret the plateau age of 165.0 ± 0.6 Ma (MSWD = 0.4, $n = 6$, $\%^{39}$Ar = 47) as the minimum cooling age for hornblende through the nominal Ar-closure window.

5.1.7. Sample CED230428A2

Sample CED230428A2 was collected from a garnet-white mica-hornblende block with minor rutile (mantled by titanite) and quartz as well as cm-scale anastomosing epidote veins from Punta Prieta Quarry (Figures 2 and 8f). White-mica in the sample shows textural association with the epidote veins. Like the other blocks from the same locality, it has a partial chlorite-actinolite-serpentinite schist rind that is enveloped in well-foliated meta(volcani-)clastic blueschists. An aliquot of amphibole (mean grain size ~350–450 μm) yielded a complicated age spectrum with the first ~10% of ^{39}Ar released yielding imprecise and erratic ages before stabilizing to a plateau age of 153 ± 24 Ma (Supporting Information S1; MSWD = 2.2, $n = 3$, $\%^{39}$Ar = 46). An aliquot of white mica (mean grain size ~250–400 μm) yields an age spectra with high-precision steps that fluctuate between 168 and 165 Ma and produce an integrated age of 167.3 ± 0.1 Ma ($n = 22$).

5.1.8. Sample CED230424B1

Sample CED230424B1 comes from a 2-3 m-scale block of glaucophane-lawsonite-white mica-quartz schist, with minor titanite, in medium-grained siliciclastic-matrix of unit PP3 (Figures 2 and 8g). The block probably records relatively low peak metamorphic temperatures (<~325°C assuming pressures ≤10 kbar) based on the stability of lawsonite (Tsujimori & Ernst, 2014). An aliquot of intergrown white mica (mean grain size ~50–150 μm) and glaucophane yields a relatively simple age spectra with monotonic increase in ages through the first ~10% of ^{39}Ar released from 25 to 150 Ma and a sloping plateau over the remaining ~90% ^{39}Ar released from 150 to 145 Ma, resulting in an integrated age of 149.2 ± 0.6 Ma ($n = 22$). We interpret the gradual increase in ages through the low-temperature steps to most likely represent volume diffusion of ^{40}Ar* and attribute the gently sloping plateau to either recoil or mass fractionation effects (Schaen et al., 2021). Given the low temperature range of lawsonite-blueschist-facies metamorphism, we cautiously interpret the integrated age of 149.2 ± 0.6 Ma as the age of white mica and glaucophane growth/recrystallization during prograde to peak metamorphism.

5.2. Matrix Descriptions and Detrital Zircon U-Pb Results

Here we describe the field context and lithology of six metasedimentary rocks sampled across two different areas of Cedros Island and report the results of 1,553 zircon U-Pb analyses from these rocks (Figure 9). The youngest age modes in all six samples are Cretaceous and a vast majority of analyses (90%) are Mesozoic. With only a few exceptions, the Mesozoic grains yield U/Th ratios <10 and exhibit simple oscillatory or sector zoning indicating a magmatic origin (Corfu, 2003; Hoskin & Schaltegger, 2003). We do not interpret any of the zircon to have formed due to high-pressure metamorphism in the Cedros subduction complex, and thus, all of the age results presented here are treated as results of detrital zircon analyses. Summaries of sample locations, lithology, and geochronologic results are provided in Table 1.

5.2.1. Sample CED230428B2

Sample CED230428B2 was collected from fine-grained, well-foliated sodic-calcic (blue-green) amphibole-quartz-white mica schist of unit PP1 at Punta Prieta (Figures 2 and 5a). Sixty-two analyses yield ages between 1.9 Ga and 87 Ma (81% Mesozoic grains), with a dominant Late Cretaceous age mode that defines a MLA of 92.5 ± 1.1 Ma and a YSP age of 87.9 ± 1.8 Ma (Figure 9a; MSWD = 0.47, $n = 3$). Due to the relatively low number of analyses for this sample (due to low zircon yield during mineral separation), these ages may overestimate the MDA and should be treated with caution.

5.2.2. Sample CED230421E2

Sample CED230421E2 was collected from medium-grained micaceous metasandstone matrix of unit PP2 (Figures 2 and 6b). Extracted zircons were almost all euhedral or very slightly abraded/rounded. 302 of 303

19449194, 2026, 4, Downloaded from https://agupubs.onlinelibrary.wiley.com/doi/10.1029/2025TC009340, Wiley Online Library on [01/06/2026]. See the Terms and Conditions (https://onlinelibrary.wiley.com/terms-and-conditions) on Wiley Online Library for rules of use; OA articles are governed by the applicable Creative Commons License

(99.7%) of the analyses yield ages between 84 and 68 Ma, with a dominant unimodal age mode that defines a MLA of 70.9 ± 0.4 Ma and a YSP age of 73.4 ± 0.2 Ma (Figure 9b; MSWD = 1, $n = 280$). One older grain yielded an age of 216 Ma.

5.2.3. Sample CED230420F1

Sample CED230420F1 was collected from a medium-grained metasandstone in unit PP3 on the northeast end of the Punta Prieta Ridge (Figure 2). 291 analyses yielded ages between 2.7 Ga and 95 Ma (87% Mesozoic grains) with a dominant Late Cretaceous age mode that defines a MLA of 96.0 ± 1.6 Ma and a YSP age of 96.4 ± 1.5 Ma (Figure 9c; MSWD = 0.97; $n = 3$).

5.2.4. Sample CED230424D1

Sample CED230424D1 is a medium- to coarse-grained metagreywacke with stretched blueschist pebbles collected from map unit PP3 in an extensional shear zone directly beneath unit sp (Figures 2 and 4b). 297 analyses yielded ages between 2.8 Ga and 94 Ma (93% Mesozoic grains), with a dominant mid-Cretaceous age mode that defines a MLA of 98.5 ± 0.5 Ma and a YSP age of 97.5 ± 0.5 (Figure 9d; MSWD = 1, $n = 40$).

5.2.5. Sample CED230422E1

Sample CED230422E1 was collected from a medium-grained lawsonite- and blueschist-bearing quartz-lithic-rich metagreywacke from the southwestern corner of Cedros Island near the fishing camp of El Wayley (Figure 1b). This locality occupies the same general structural position as the Punta Prieta PP1-3 nappes, beneath the serpentinite roof zone, but is spatially separated from the these units and may represent still another nappe. 296 analyses yield ages between 3.3 Ga and 83 Ma (86% Mesozoic grains), with a dominant multimodal age group between 119 and 83 Ma (68% of analyzed grains) that define a MLA of 85.5 ± 1.0 Ma and a YSP age of 85.1 ± 0.5 Ma (MSWD = 0.98, $n = 20$). A subsidiary non-gaussian Middle Jurassic to Early Cretaceous age mode is defined by analyses with ages between 175 and 126 Ma (18% of analyzed grains).

5.2.6. Sample CED230423A1

Sample CED230423A1 was collected from coarse-grained glaucophane-bearing metasandstone from the southwestern corner of Cedros Island near the fishing camp of San Agustin (Figure 1b), part of the same subduction-complex exposure as CED230422E1, and geographically distinct from the Punta Prieta Ridge localities. 304 analyses yielded ages between 2.0 Ga and 81 Ma (84% Mesozoic grains), with a dominant bi-multimodal age group between 111 and 81 Ma (81% of grains analyzed) and a subsidiary non-gaussian age mode between 178 and 118 Ma (12% of grains analyzed). The analyzed grains yield a MLA of 84.9 ± 0.5 Ma and the youngest two grains yield a YSP age of 81.9 ± 1.7 Ma (MSWD = 0.93, $n = 2/304$).

6. Discussion

6.1. Assembly and Exhumation of Subduction Assemblages

Subduction assemblages of Punta Prieta Ridge are structurally organized into four mappable fault-bounded units composed of, from structurally highest to lowest, a serpentinite mélange roof zone (sp), coherent blue-green (sodic-calcic) amphibole-bearing schists (PP1), metasedimentary-matrix mélange (PP2), and lawsonite-albite-facies imbricated ocean plate stratigraphy (PP3) which is regionally coherent but locally exhibits distinct meter- to decameter-scale horizons of mélange (block-in-matrix texture) and transposed ocean plate stratigraphy (broken formation). Siliciclastic rocks within these nappes yielded MDAs between ca. 92 and 72 Ma, suggesting that a majority of the subduction complex material was accreted over ~20 million years. Similar to the Franciscan subduction complex, high-pressure blocks from the overlying serpentinite roof zone and from intra-formational metasedimentary matrix mélanges make up volumetrically minor portions of the complex but record older and longer histories of subduction accretion and metamorphism. In the following sections, we propose models for the accretion, metamorphism, and exhumation of high-pressure rocks from oldest to youngest and structurally highest to lowest (Figure 10).

19449194, 2026, 4, Downloaded from https://agupubs.onlinelibrary.wiley.com/doi/10.1029/2025TC009340, Wiley Online Library on [01/06/2026]. See the Terms and Conditions (https://onlinelibrary.wiley.com/terms-and-conditions) on Wiley Online Library for rules of use; OA articles are governed by the applicable Creative Commons License

10.1029/2025TC009340

19449194, 2026, 4, Downloaded from https://agupubs.onlinelibrary.wiley.com/doi/10.1029/2025TC009340, Wiley Online Library on [01/06/2026]. See the Terms and Conditions (https://onlinelibrary.wiley.com/terms-and-conditions) on Wiley Online Library for rules of use; OA articles are governed by the applicable Creative Commons License

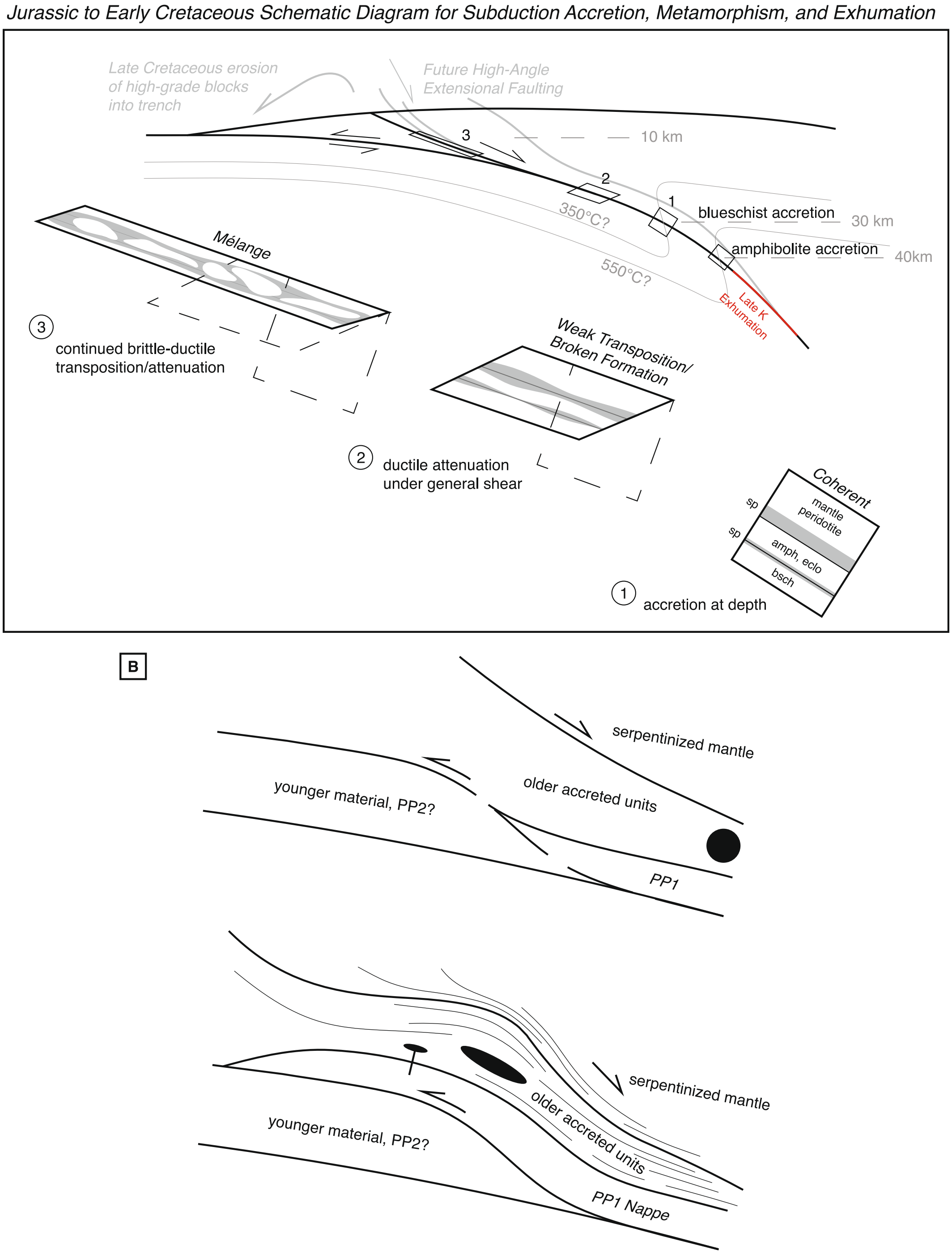

Figure 10. Conceptual diagrams showing model for subduction accretion, metamorphism, and exhumation of high-pressure rocks in the Cedros subduction complex. (a) Schematic cross-section through Middle Jurassic to Early Cretaceous forearc of Baja California showing accretion of amphibolite and blueschist facies rocks at the base of the wedge and subsequent exhumation and attenuation along constrictional shear zone in three steps. Isotherms are speculative and based on previously published P-T estimates of amphibolite and blueschist blocks (Baldwin & Harrison, 1992; Gonzalez & Baldwin, 2019) and generalized thermal models of subduction zones (Peacock, 1996; van Keken & Wilson, 2023). Mélange formation and attenuation of originally coherent structures depicted through progressive general shear of a unit cell. The unit cell is deformed under equal pure and simple shear after Teyssier et al. (2010) and conserves area for simplicity. However, we note that most subduction complex rocks from this study exhibit evidence for large volume solution mass transfer, suggesting that conservation of mass is not realistic or necessary for the model. Abbreviations: sp = serpentinite, bsch = blueschist, amph = amphibolite, eclo = eclogite. (b) Zoomed-in cross-section of the subduction interface during metamorphism and accretion of younger units (PP2?) below older high-pressure schists (PP1). Basal contraction and underplating paired with extension and attenuation along the serpentinite roof zone flattens and attenuates the older, higher nappes. Kinematics of extensional structures are drawn within the cross-section for clarity, but extension was likely strike-parallel (in and out of the plane of section) based on kinematic data from the extensional roof zone.

19449194, 2026, 4, Downloaded from https://agupubs.onlinelibrary.wiley.com/doi/10.1029/2025TC009340, Wiley Online Library on [01/06/2026]. See the Terms and Conditions (https://onlinelibrary.wiley.com/terms-and-conditions) on Wiley Online Library for rules of use; OA articles are governed by the applicable Creative Commons License

6.2. Serpentinite Roof Zone: Origin of High-Pressure Blocks and Serpentinite Mélange Formation

Meters- to hundreds of meters-thick shear zones of serpentinite-matrix mélanges that separate overlying ophiolites and forearc basin strata from underlying higher-P accretionary assemblages are common first-order features in subduction complexes and suture zones around the world (e.g., the Tehama-Colusa mélange of the Franciscan, the Zangbo mantle thrust of southern Tibet, etc.; Ding et al., 2005; Guilmette et al., 2012; Shervais et al., 2011). These serpentinite-matrix mélange shear zones typically host intermixed blocks with very different P-T-t histories from both structurally overlying and underlying rocks (e.g., Hopson & Pessagno, 2005). The high-pressure blocks in these zones are interpreted as metamorphosed remnants of the subducted slab, but it is unclear whether they represent material that was randomly sampled and exhumed in a low-viscosity return-flow-style subduction channel (e.g., Gerya et al., 2002) operating throughout the lifetime of a subduction zone, or whether they represent once coherent sequences that were attenuated during progressive shear along the slab-mantle interface and exhumed by either extensional, erosional, and/or diapiric processes (Wakabayashi, 2019). The juxtaposition of high-pressure, schistose blueschist-bearing rocks below basically non-metamorphosed upper plate material suggests that in at least the latter phases of deformation, serpentinite roof zones accommodate significant extension and exhumation (>20 km vertical motion) that can explain pressure differences in excess of 4 kbar (Platt, 1987).

Our mapping and field observations of the serpentinite roof zone enveloping Punta Prieta Ridge show a lithologic gradient from a structurally high, relatively coherent harzburgite to lower zones composed of >80% high-pressure blocks hosted in a serpentinite-schist matrix (locally with chlorite-actinolite-serpentine, Figures 3a–3d). We suggest that the zone formed mainly by brittle-ductile extension that attenuated the overlying serpentinized mantle and underlying high-pressure rocks in multiple cycles over the life of the subduction zone (Figure 10a).

The first cycle is recorded by high-grade blocks concentrated at the base of the roof zone and dispersed throughout the lower nappes, which may represent a dismembered metamorphic sole (notably, [garnet ± epidote] amphibolites) of the Cedros Ophiolite (not mapped at Punta Prieta Ridge, but perhaps represented by the serpentinized harzburgite that structurally overlies the high-grade block mélange) or some other highly attenuated coherent sequence of rocks originally accreted to the base of the serpentinite mantle wedge (Figure 10a). The similar ca. 172–171 Ma white mica and hornblende $^{40}Ar/^{39}Ar$ cooling ages for the three high-grade blocks analyzed from this zone suggest that the blocks were rapidly cooled through temperatures of ~550°C to 360°C (see Rutte et al. (2020) and references there-in), coincident with the formation of the structurally overlying ca. 173 Ma Cedros Island Ophiolite (Kimbrough & Moore, 2003). Garnet-amphibolite blocks from PP1 matrix yield similar ages of ~167–164 Ma, when upper-plate extension was still active (recorded in the Choyal Formation, Figure 11a; Kimbrough & Moore, 2003), suggesting that they were exhumed during the same continuous event and were later eroded and recycled into the younger and lower-grade matrix. We observe a similar overlap in ages between younger blueschist blocks in the serpentinite roof zone and underlying PP3 metasedimentary-matrix mélange, which record sodic amphibole + white mica $^{40}Ar/^{39}Ar$ cooling ages of 144 and 149 Ma, respectively. We tentatively suggest that these Early Cretaceous blueschists record progressive underplating below the previously accreted Jurassic amphibolites when the wedge was in a state of critical taper and exhumation was controlled mainly by internal deformation (underplating) and erosion at the surface. Retrogression of older, amphibolite blocks through the blueschist facies is supported by the observation of blue amphibole rims growing over hornblende/actinolite cores in some samples (Baldwin & Harrison, 1992). The transition from amphibolite to blueschist-facies metamorphism may represent cooling of the subduction interface but more thermobarometric data are needed to test this hypothesis and the timescales over which such cooling may have occurred (e.g., Bonnet et al., 2024; Cordova et al., 2019; Cunetta et al., 2025; Rutte et al., 2020).

After accretion of Early Cretaceous blueschists, the forearc upper plate underwent an episode of extension as recorded by deposition of the Tithonian to Valanginian arc-proximal volcanogenic strata and intercalated olistostromes that are interpreted to have been deposited in local rift basins on Cedros Island (the Coloradito and Eugenia Formations, Figure 11a; Kimbrough & Moore, 2003). We suggest that at this time, abrupt regional decreases in plate convergence velocities (from >100 to <50 km/myr, Figure 11b; Engebretson et al., 1984) caused the wedge to become gravitationally unstable. As a result, the forearc extended and high-pressure rocks (garnet amphibolites and blueschists) were exhumed rapidly to shallow crustal levels along brittle-ductile shear zones that accommodated extension and attenuation of the wedge. Exhumational mode switching from slow basal contraction and surface erosion to rapid extension and attenuation is supported by multidomain diffusion

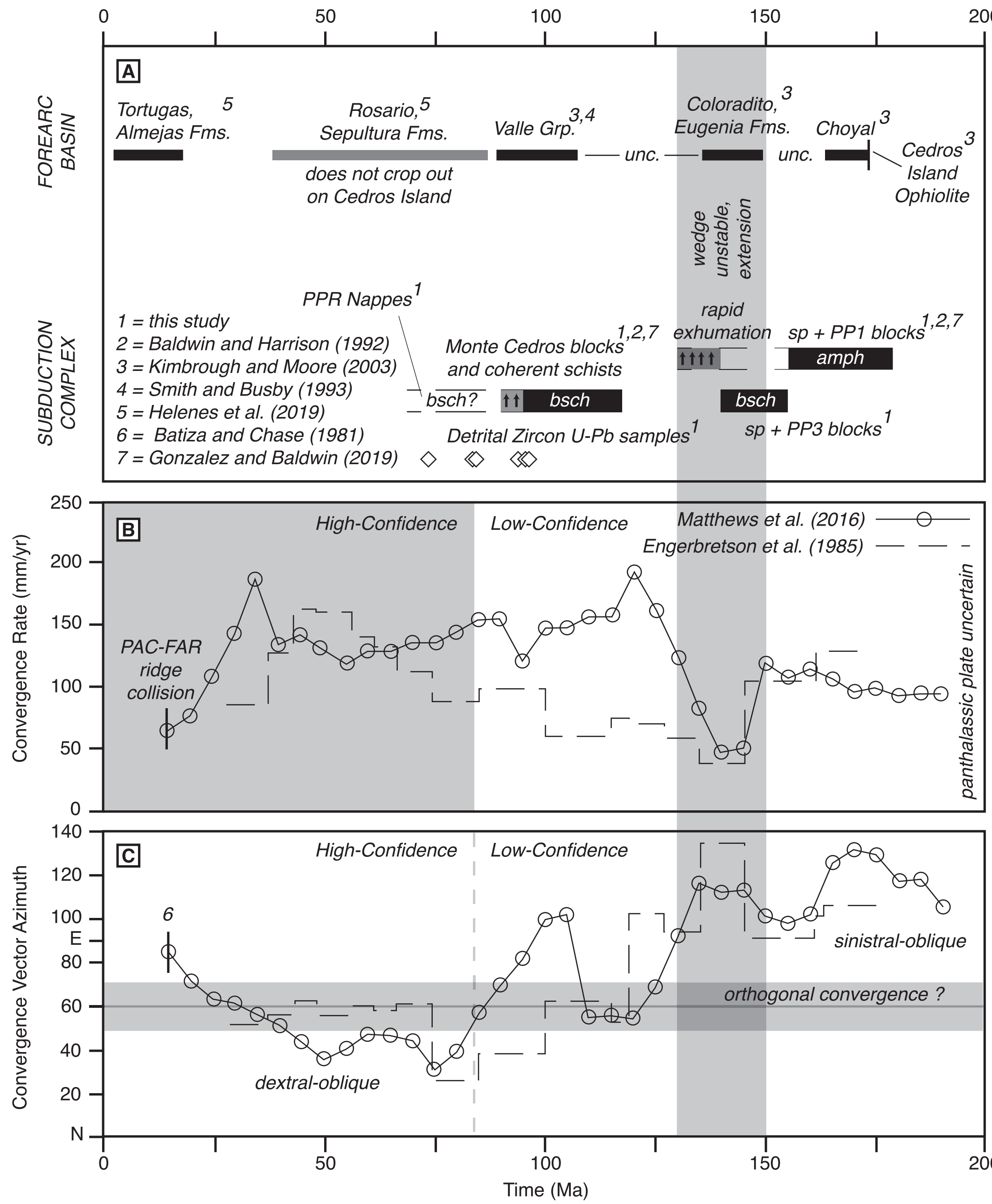

Figure 11. Diagram showing geochronology of subduction complex rocks on Cedros Island compiled from this and previous studies in-relation to forearc stratigraphy and regional plate kinematics. Plate kinematics calculated in 5 Myr intervals from 190 to 15 Ma for a reference point at 28°N, 115°W between the Farallon (plate ID = 902) and North American (Mexico; plate ID = 104) plates using the global plate circuit reconstruction of Matthews et al. (2016) in GPlates (Müller et al., 2018). Convergence obliquity determined by assuming the plate margin of the field area has had an orientation of N30W ± 10° (horizontal gray line and error bar in panel c) since Middle Jurassic time. Note how formation and exhumation of high-pressure rocks is coeval with major phases of extension in the forearc and changes in plate convergence.

modeling (MDD) on white mica $^{40}Ar/^{39}Ar$ step heating experiments from an epidote-amphibolite block in the PP1 mélange which shows that high-pressure rocks were slowly cooled at rates of ~3°C/Myr (~0.12 km/Myr) until ca. 140 Ma, after which they were more rapidly exhumed to shallow crustal levels (<100°C) at rates of ~25°C/Myr (~1 km/Myr) (Gonzalez & Baldwin, 2019).

19449194, 2026, 4, Downloaded from https://agupubs.onlinelibrary.wiley.com/doi/10.1029/2025TC009340, Wiley Online Library on [01/06/2026]. See the Terms and Conditions (https://onlinelibrary.wiley.com/terms-and-conditions) on Wiley Online Library for rules of use; OA articles are governed by the applicable Creative Commons License

We envision that progressive shear during exhumation of the rocks would transpose the original fault sequence from (a) a coherent duplex with an inverted metamorphic gradient underplated at the base of the serpentinite mantle (possibly the base of the Cedros Island Ophiolite, i.e., a metamorphic sole) to (b) a broken formation/weakly transposed slab of material where coherent schists are boudinaged in serpentinite-matrix to (c) a tectonic mélange where full transposition achieved by a combination of pure and simple shear completely disrupted the original fault zone stratigraphy (Figure 10a). The latter stages of this extensional attenuation/exhumation of the high-pressure rocks would have happened in the mid- to upper-crustal portions of the wedge concurrently with continued underplating of material in deeper portions of the wedge, perhaps represented by mid-Cretaceous coherent blueschists exposed at Monte Cedros (Figure 10b; st1 and st2 of Sedlock (1988c)). These schistose blueschists structurally overlie the rocks of Punta Prieta Ridge and yield white mica $^{40}Ar/^{39}Ar$ cooling ages of ca. 112 to 94 Ma (Baldwin & Harrison, 1989, 1992). Blueschist blocks from the San Carlos shear zone (serpentinite roof zone below the Cedros Island ophiolite on the north end of Monte Cedros, which we interpret as equivalent to the serpentinite roof zone of Punta Prieta Ridge) yield white mica $^{40}Ar/^{39}Ar$ age spectra with identical ages, and multi-domain diffusion modeling on two blocks suggest that they underwent rapid cooling compared to estimates from the coeval underlying coherent sequences (Gonzalez & Baldwin, 2019). These results suggest that this portion of the serpentinite roof zone at Monte Cedros may have accommodated a younger but similar phase of extensional exhumation and attenuation as interpreted for Punta Prieta Ridge. By at latest ca. 94 Ma, some proportion of the serpentinite mélange would have been exposed at the surface to erosion, allowing for sedimentary recycling of the Middle Jurassic to Early Cretaceous blocks (now olistoliths) into Late Cretaceous sediment entering the trench.

6.3. Accretion and Metamorphism of Coherent Units and Origin of Sedimentary-Matrix Mélange

Sodic-calcic amphibole-quartz-white mica schists of the structurally highest coherent nappe of Punta Prieta Ridge (PP1) yield a detrital zircon MDA of ca. 92 Ma ($n = 62$), requiring that the protolith material was deposited into the trench after this time. At ca. 95 Ma, the volcanic arc was highly active and rapidly eroding material into the forearc (Kimbrough et al., 2001), so we infer that the zircon MDA closely approximates the true depositional age of the rock. Convergence rates between the Farallon and North American plates are also thought to have been very high during this time (>100 km/Myr) (Engebretson et al., 1984; Matthews et al., 2016), requiring <1 Myr for material to be subducted to depths of around 30–40 km (~10 kbar). Early recumbent folds, mesoscale duplexes, and S-C-C' fabrics developed in schistose lithologies of PP1 may have formed by contractional deformation at the base of the wedge during or shortly after this time (Figure 5).

Garnet-amphibolite blocks hosted in PP1 sodic-calcic amphibole-schist matrix are higher-grade and yield considerably older $^{40}Ar/^{39}Ar$ cooling ages of 167 to 164 Ma compared to the ca. 92 Ma matrix protolith. These combined data sets show that the blocks record thermal histories of metamorphism and exhumation in the subduction complex that significantly predate burial and metamorphism of the host matrix, which is incompatible with return flow models for block exhumation (Krohe, 2017). Thus, we interpret the garnet-amphibolite blocks in PP1 as olistoliths that were exhumed to the surface during previous phases of extension in the wedge and deposited into the trench alongside the protolith of the sodic-calcic amphibole-quartz-white mica schists as a sedimentary mélange (Wakabayashi, 2017).

Micaceous metasandstone-matrix of the structurally underlying PP2 mélange yields a robust MDA of ca. 72 Ma, ~20 Myr younger than the PP1 sodic-calcic amphibole-schist protolith. This gap in time may represent either a period of non-accretion (perhaps due to changes in wedge geometry or sediment supply to the trench), subduction erosion, or may simply reflect lack of geochronological analyses through the full structural thickness of the PP1 nappe. It is also possible that the relatively low number of analyses ($n = 62$) for our PP1 sample did not include younger zircon actually present in the rock and thus has resulted in an overestimate of the MDA for the unit. Two detrital zircon samples collected from subduction complex rocks at Cabo San Agustin (Figure 1b) yield MDAs of 86 and 85 Ma, indicating that subduction accretion was ongoing in other portions (~10 km away) of the wedge during the interval between the PP1 and PP2 samples dated at Punta Prieta Ridge. These differences in MDAs among nappes and subduction complex exposures suggest both spatial and temporal heterogeneity of accretion in the Cedros subduction complex.

Based on the tabular outcrop of PP2 mélange and parallelism of internal fabric with the bounding faults, we interpret the unit as having a strong deformational overprint (Festa et al., 2019; Wakabayashi, 2025) but interpret

19449194, 2026, 4, Downloaded from https://agupubs.onlinelibrary.wiley.com/doi/10.1029/2025TC009340, Wiley Online Library on [01/06/2026]. See the Terms and Conditions (https://onlinelibrary.wiley.com/terms-and-conditions) on Wiley Online Library for rules of use; OA articles are governed by the applicable Creative Commons License

19449194, 2026, 4, Downloaded from https://agupubs.onlinelibrary.wiley.com/doi/10.1029/2025TC009340, Wiley Online Library on [01/06/2026]. See the Terms and Conditions (https://onlinelibrary.wiley.com/terms-and-conditions) on Wiley Online Library for rules of use; OA articles are governed by the applicable Creative Commons License

the main mixing mechanism that formed the block-in-matrix fabric to have been sedimentary, where high-pressure amphibolite and blueschist blocks were sourced as olistoliths from the eroded serpentinite roof zone in a similar fashion to amphibolite blocks in PP1. This inference is based on several key field observations: (a) that the exotic blocks in PP2 do not contain any of the pervasive lithologies of overlying PP1 (lower-grade sodic-calcic amphibole-quartz-schists, calcschists, stretch pebble conglomerates, etc.) or underlying PP3 (ribbon chert, pillowed metabasite, fine-grained greywacke, etc.), (b) blocks exhibit a high degree of weathering relative to their host matrix, indicating that they were weathered before being incorporated into the matrix, and (c) fabrics within the blocks are discordant with fabrics in the matrix (if any are present) (Wakabayashi, 2025). Thus, we interpret the PP2 mélange as a thrust nappe that localized strain into the relatively weak siliciclastic cover of the subducting oceanic plate ca. 70 Ma when material from the roof zone was still eroding into the trench.

Siliciclastic matrix mélange horizons of PP3 host abundant blueschist detritus, which show evidence at many scales for origin as sedimentary clasts/blocks (Figure 7) and yield older detrital zircon MDAs of 98 and 96 Ma. Given the abundance of younger Late Cretaceous zircon U-Pb grains in all our other samples, and their absence in the PP3 samples, these >20 Myr older MDAs likely closely approximates the true depositional age. However, the inference that PP3 is much older than the structurally overlying sediments of PP2 is at odds with simple models that predict progressive accretion of younger material structurally downward in accretionary complexes (e.g., Žák et al., 2020). Perhaps the simplest explanation of the older MDAs at the bottom of the exposed structural pile, and the interpretation we favor, is that the nappes formed via out-of-sequence thrusting (e.g., Morley, 1988), where deformation shifted back into the rear of the wedge, either reactivating an existing structure or breaking a new splay that carried the younger and more recently accreted PP2 material over the older PP3. Such deformation is common in accretionary wedges when addition of new material at the base of the wedge outpaces erosion at the surface and taper reaches a supercritical state (Haq, 2012). It is also possible to explain the younger-on-older nappe sequence via in-sequence duplexing of older, stratigraphically deeper material beneath PP2, but this would require that relatively coarse-grained blueschist-bearing material had accumulated on the subducting plate for >25 Myr before subducting. If we assume continuous, relatively rapid convergence (>100 mm/yr) occurred along the western margin throughout the Late Cretaceous, as is predicted in plate kinematic models (Figure 11c), this would likely only be possible by the oblique subduction of a long-lived fan complex (e.g., similar in scale to the subduction of the Bengal Fan in Sumatra or the Zodiac Fan in southern Alaska). The implication of such a long-lived, large volume fan is that high-pressure blocks and other detritus now preserved in subduction complexes along the western margin may have originated elsewhere before being exhumed, eroded, and deposited back onto the subducting plate which carried it to its final resting place. We highlight this possibility to illustrate the complexities that sedimentary recycling of blocks may introduce toward interpreting the long-term metamorphic history of a subduction complex along a given portion of a convergent margin. More work is needed to determine the kinematic sequence of nappe assembly on Cedros Island, but for now we tentatively assume that the recycled blocks came from nearby sources and that the age sequence observed at Punta Prieta Ridge is an indication of out-of-sequence faulting within the wedge after ca. 70 Ma.

6.4. Detrital Zircon Provenance

Detrital zircon U-Pb age spectra indicate that sediment in the Cedros Island subduction complex was predominantly derived from nearby Mesozoic arc plutonic and volcanic rocks with minor contributions of older Paleozoic and Proterozoic detritus. A composite Mesozoic age spectrum combining data from the six samples analyzed here correlates well with compiled igneous zircon U-Pb crystallization ages from the Peninsular Ranges Batholith (PRB; Figure 12; Contreras-López et al., 2021). The exception are post-90 Ma zircons, which make up ∼26% of the analyzed grains and provide constraints on the MDAs of samples. These younger zircons do not have any known source in the Peninsular Arc and were probably derived from more inboard sources following eastward migration of the arc during the Late Cretaceous. Based on broad similarities in reported igneous zircon U-Pb crystallization ages, we tentatively suggest that the younger zircons were derived from the Sonoran Batholith (Figures 1 and 12), which is interpreted to be the locus of Late Cretaceous arc magmatism in the Mexican Cordillera (Ramos-Velázquez et al., 2008). After restoring Cenozoic rifting and opening of the Gulf of California, arc volcanic and plutonic rocks of the Sonoran Batholith restore to within ∼200 km of the Cedros Island subduction complex (Ferrari et al., 2013).

Pre-Mesozoic grains make up only ∼8% of the analyzed zircons ($n = 129$) which limits our ability to differentiate provenance signals from unique cratonic and orogenic sources (e.g., Laurentian vs. peri-Gondwanan vs. Ouchita-

10.1029/2025TC009340

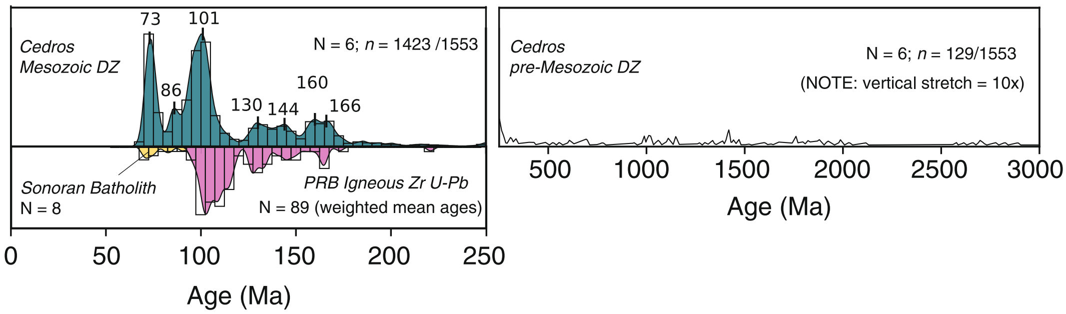

Figure 12. Composite detrital zircon kernel density estimate (KDE) plot including all analyses from this study compared against mirrored KDE plot of igneous zircon U-Pb weighted mean ages from the Peninsular Ranges Batholith (Contreras-López et al., 2021) and the coastal Sonoran Batholith (Ramos-Velázquez et al., 2008). For clarity, the pre-Mesozoic detrital zircon KDE is stretched vertically by a factor of 10.

Marathon Belt; Centeno-García, 2017). However, the lack of older zircons is consistent with detrital zircon data reported for time-equivalent metagreywackes along strike in the Franciscan (Apen et al., 2021) and from underplated schists of the southern California Borderlands (A. D. Chapman, 2017). The dominance of Mesozoic zircons among these units (and relative lack of older zircons from the continental interior) suggest that sediment routing to the trench during the Late Cretaceous was dominated by erosion of the arc. This is consistent with evidence for rapid exhumation of the Peninsular Ranges Batholith between ca. 90 and 50 Ma and contemporaneous increased supply of arc-derived sand to the forearc (Grove et al., 2003; Jiang & Lee, 2019; Kimbrough et al., 2001).

6.5. Implications for Cordilleran Subduction Dynamics

The transition from relatively high-T/P amphibolite- and eclogite-facies metamorphism during the Middle Jurassic coeval with SSZ ophiolite generation in the upper plate to subsequent accretion/exhumation of blueschists through the Early Cretaceous is a common geological history recorded by forearc assemblages along the North American Cordilleran margin. The Middle Jurassic ages reported here are indistinguishable from ages reported by Baldwin and Harrison (1992) for garnet-amphibolite, epidote-amphibolite, and eclogite blocks collected from the equivalent serpentinite-matrix mélange roof zone at other localities in the Cedros-Vizcaíno region and are coincident with the formation of the structurally overlying ca. 173 Ma Cedros Island Ophiolite (Kimbrough & Moore, 2003). In the Franciscan, high-pressure blocks structurally underlie the ca. 172–161 Ma Coast Range Ophiolite (Hopson et al., 2008; Shervais et al., 2005) and yield metamorphic cooling ages that indicate early formation and exhumation of amphibolites and eclogites from 176 to 143 Ma and coeval and younger exhumation of blueschists from 155 to 134 Ma (Rutte et al., 2020). A similar history is recorded in a coherent sequence of accreted nappes in the Northwest Cascades of northern Washington, which record the transition from Early Jurassic amphibolite-facies metamorphism to Early Cretaceous blueschist metamorphism coeval with and after formation of the overlying Middle Jurassic Fidalgo (ca. 171 Ma) and Ingalls (ca. 164 Ma) ophiolites (Cordova et al., 2019). Rutte et al. (2020) proposed that this exhumation pulse in the Franciscan may be related to the sinistral-oblique subduction of a spreading ridge based on regional north-to-south younging observed in their compiled block data from California alone. However, the relative synchroneity of these records over >3,000 km along-strike suggests that the event was probably controlled by larger-scale processes.

Previous studies have suggested that the Middle Jurassic SSZ ophiolites in the North American Cordillera and their underlying high-grade rocks (amphibolites and eclogites) reflect upper plate rifting and elevated geothermal gradients during subduction initiation, with analogy to the well-studied Eocene Izu-Bonin forearc ophiolite system in the western Pacific and high-grade metamorphic sole-SSZ ophiolite pairs in the Tethyan realm (Cordova et al., 2019; Guilmette et al., 2018; Mulcahy et al., 2018; Shervais, 2001; Stern & Bloomer, 1992). However, in the Cedros-Vizcaíno region, older Late Triassic suprasubduction zone ophiolites on the Vizcaíno Peninsula occupy the same structural-stratigraphic position as the Middle Jurassic Cedros Island ophiolite and appear to be part of the same forearc upper plate, suggesting that east-dipping subduction along the continental margin initiated by at least ca. 220 Ma, and perhaps earlier (Boschman et al., 2018; Busby, 2004; Kimbrough & Moore, 2003). Although it is possible that the Middle Jurassic ophiolite and the garnet-amphibolite blocks on

19449194, 2026, 4, Downloaded from https://agupubs.onlinelibrary.wiley.com/doi/10.1029/2025TC009340, Wiley Online Library on [01/06/2026]. See the Terms and Conditions (https://onlinelibrary.wiley.com/terms-and-conditions) on Wiley Online Library for rules of use; OA articles are governed by the applicable Creative Commons License

19449194, 2026, 4, Downloaded from https://agupubs.onlinelibrary.wiley.com/doi/10.1029/2025TC009340, Wiley Online Library on [01/06/2026]. See the Terms and Conditions (https://onlinelibrary.wiley.com/terms-and-conditions) on Wiley Online Library for rules of use; OA articles are governed by the applicable Creative Commons License

Cedros Island represent a (dismembered) sole-ophiolite pair formed during re-initiation of the same subduction system (e.g., after a strike-slip interlude), there is no regional geologic evidence for a >50 m.y.r. hiatus in convergence.

Farther north, there are also earlier records of subduction along the continental margin. These include emplacement of Late Triassic plutons in North American basement of the eastern Sierra Nevada (e.g., Barth et al., 2011) and the preservation of Late Triassic blueschists and amphibolites in the Sierran Foothills (i.e., the Red Ant blueschist; Rutte et al., 2020), Klamath Mountains (e.g., the Stuart Fork blueschists; Goodge, 1990), and North Cascades (e.g., the Vedder and Bridge River Complexes, amphibolites and blueschists; Archibald et al., 1990; Armstrong et al., 1983). Unlike the Cedros-Vizcaíno region, the Triassic subduction-related rocks in these areas are commonly interpreted as products of separate, older subduction zones (Cunetta et al., 2025; Goodge, 1995; Schweickert & Cowan, 1975; Wakabayashi et al., 2023) that terminated prior to the initiation and onset of the main Jurassic-Paleogene Cordilleran subduction system (e.g., DeCelles, 2004). These older subduction complexes (sometimes with and sometimes without time correlative structurally overlying SSZ ophiolites) provoke an important series of questions: do coeval subduction complex and ophiolite pairs in the geologic record always represent initiation of unique subduction zones? Or could they represent other non-steady state processes related to upper plate rifting and elevated thermal conditions along the subduction interface?

We suggest that rather than marking east-dipping subduction initiation, the shared Early to Middle Jurassic geologic history across much of the western margin could reflect a regional kinematic shift to sinistral-oblique subduction driven by the initial break-up of Pangea. From ca. 200 to 150 Ma, North America is thought to have moved northward during the opening of the central Atlantic, which would have resulted in sinistral-oblique convergence vectors that deviated >45° from normal to the reconstructed trench margin (Figure 11c). Moderate to highly-oblique subduction systems on the modern Earth, such as the central and western Sumatra-Java system exhibit upper plate rifting of transitional arc-ophiolite lithosphere, strike-slip faulting within the arc, and stretching of upper-plate arc lithosphere parallel to the trench (e.g., the Andaman sea region; Curray, 2005; De Saint Blanquat et al., 1998). These observations are compatible with recent kinematic reconstructions for rifting and formation of Middle Jurassic suprasubduction zone ophiolites in the US Cordillera, for which regional isotopic age trends and paleomagnetic studies on sheeted dike swarms suggest formation by north-south (i.e., trench-parallel) spreading (Arkula et al., 2022). Because subduction zone thermal structures are largely thought to be the product of the age of the subducting lithosphere and the rates of plate convergence (Holt & Condit, 2021; Peacock, 1996), moderate- to highly-oblique subduction would also provide a mechanism for lowering the rates of trench-normal convergence and thus could raise the geothermal gradient of the subduction interface due to decreased refrigeration rates of the overlying forearc upper plate. 3D numerical modeling of subduction systems show that increased subduction obliquity may also increase trench-parallel flow in the mantle wedge, which could cause regional increases in the subducting slab top temperature of >200°C and theoretically facilitate the transition from previously cold (lawsonite-blueschist) to warm (amphibolite- and/or eclogite-facies) metamorphism (Plunder et al., 2018).

7. Conclusions

Subduction complex rocks of Punta Prieta Ridge are exposed in the footwalls of domal moderate- to low-angle extensional shear zones developed in a zone of serpentinite-matrix mélange that wraps around the range. The subduction complex rocks are organized in tabular, southwest-dipping fault-bounded panels that decrease in metamorphic grade and degree of strain structurally downwards to the northeast. High-pressure blocks in serpentinite- and metasedimentary-matrix mélange decrease in age and metamorphic grade structurally downward from ca. 171 to 165 Ma high-T/P amphibolites to ca. 149 to 145 Ma lawsonite- and epidote-blueschists. Detrital zircon geochronology of metasedimentary rocks from coherent nappes indicates that most of the material in the Cedros subduction complex was accreted between ca. 92 and 73 Ma, when plate convergence rates were high. We tentatively interpret a kinematic sequence of assembly for the Cedros subduction complex as follows: (a) oceanic protoliths of the high-grade blocks were originally accreted as coherent sheets at depths ~30–40 km; (b) high-grade rocks were slowly cooled during progressive underplating of blueschist-facies rocks and erosion of the overlying wedge at mid-crustal depths until ca. 140 Ma; (c) amphibolites and blueschist were rapidly exhumed together to shallow crustal levels and attenuated during Early to mid-Cretaceous constrictional extension; and finally (d) blocks of the amphibolite and blueschist were eroded at the surface and recycled back into the subduction trench as olistoliths between 92 and 73 Ma. We suggest that the common geologic history of Middle

Jurassic ophiolite formation in the upper plate and coeval high-grade (amphibolite- and eclogite-facies) metamorphism in underlying subduction complex rocks observed on Cedros and several other segments of the Cordilleran margin may reflect margin-scale changes in the thermomechanical structure of the subduction interface and gravitational stability of the forearc upper plate driven by changes in plate convergence obliquity.

Conflict of Interest

The authors declare no conflicts of interest relevant to this study.

Availability Statement

All data presented in this paper are available in a Zenodo data repository: https://doi.org/10.5281/zenodo.17978619 (Wang et al., 2026). Figures depicting age spectra and K/Ca ratios for ^{40}Ar/^{39}Ar step heating experiments were made using PyChron software of Ross (2017), available at https://github.com/NMGRL/pychron. Detrital zircon kernal density estimate plots were made using the detritalPy software of Sharman et al. (2018), available at https://github.com/grsharman/detritalPy. Igneous zircon KDE plots were made in R using the ggplot function with geom_density and geom_histogram layers from the ggplot2 library, available at https://ggplot2.tidyverse.org/ (Wickham, 2016). Convergence rate and convergence vector azimuth versus time plots were generated using the global plate circuit reconstruction of Matthews et al. (2016) in GPlates (Müller et al., 2018), available at https://www.gplates.org/.

Acknowledgments

This work was funded by NSF-EAR Grants 2127195 (Holder) and 2127229 (Kapp). We thank the CONANP "Islas del Pacífico"office (H. Toledo-Reza and V. G. Sánchez-Sotomayor) for granting research permits and J. F. Bareño-Gutiérrez for assistance during fieldwork. J. Wu is thanked for his help in generating convergence data from plate circuit reconstructions in GPlates. We also thank S. Mulcahy and M. Ibañez-Mejia for early comments on the manuscript. Finally, we thank J. Wakabayashi and an anonymous reviewer for thoughtful feedback that improved the discussion of Middle Jurassic subduction dynamics in the Cordillera and organization of the results.

References

Agard, P., Plunder, A., Angiboust, S., Bonnet, G., & Ruh, J. (2018). The subduction plate interface: Rock record and mechanical coupling (from long to short timescales). *Lithos*, *320–321*, 537–566. https://doi.org/10.1016/j.lithos.2018.09.029

Agard, P., Yamato, P., Jolivet, L., & Burov, E. (2009). Exhumation of oceanic blueschists and eclogites in subduction zones: Timing and mechanisms. *Earth-Science Reviews*, *92*(1–2), 53–79. https://doi.org/10.1016/j.earscirev.2008.11.002

Apen, F. E., Wakabayashi, J., Day, H. W., Roeske, S. M., Souders, A. K., & Dumitru, T. A. (2021). Regional-scale correlations of accreted units in the Franciscan Complex, California, USA: A record of long-lived, episodic subduction accretion.

Archibald, D., Schiarizza, P., & Garver, J. (1990). ^{40}Ar/^{39}Ar evidence for the age of igneous and metamorphic events in the Bridge River and Shulaps complexes, southwestern British Columbia. In *Geological fieldwork, 1991*.

Arkula, C., Lom, N., Wakabayashi, J., Rea-Downing, G., Qayyum, A., Dekkers, M. J., et al. (2022). The forearc ophiolites of California (USA) formed during trench-parallel spreading: Kinematic reconstruction of the western USA Cordillera since the Jurassic.

Armstrong, R., Harakal, J., Brown, E., Bernardi, M., & Rady, P. (1983). Late Paleozoic high-pressure metamorphic rocks in northwestern Washington and southwestern British Columbia: The Vedder Complex. *Geological Society of America Bulletin*, *94*(4), 451–458. https://doi.org/10.1130/0016-7606(1983)94<451:lphmri>2.0.co;2

Baldwin, S. L., & Harrison, T. M. (1989). Geochronology of blueschists from west-central Baja California and the timing of uplift in subduction complexes. *The Journal of Geology*, *97*(2), 149–163. https://doi.org/10.1086/629291

Baldwin, S. L., & Harrison, T. M. (1992). The PTt history of blocks in serpentinite-matrix mélange, west-central Baja California. *Geological Society of America Bulletin*, *104*(1), 18–31. https://doi.org/10.1130/0016-7606(1992)104<0018:tpttho>2.3.co;2

Barth, A., Walker, J., Wooden, J., Riggs, N., & Schweickert, R. (2011). Birth of the Sierra Nevada magmatic arc: Early Mesozoic plutonism and volcanism in the east-central Sierra Nevada of California. *Geosphere*, *7*(4), 877–897.

Beaumont, C., Jamieson, R. A., Butler, J., & Warren, C. (2009). Crustal structure: A key constraint on the mechanism of ultra-high-pressure rock exhumation. *Earth and Planetary Science Letters*, *287*(1–2), 116–129. https://doi.org/10.1016/j.epsl.2009.08.001

Bonnet, G., Apen, F., Soret, M., Noel, J., Caron, B., Ninkabou, D., et al. (2024). Seamount subduction dynamics and long-term evolution of the Franciscan active margin. *Tectonics*, *43*(3), e2023TC008084. https://doi.org/10.1029/2023tc008084

Boschman, L. M., Van Hinsbergen, D. J. J., Kimbrough, D. L., Langereis, C. G., & Spakman, W. (2018). The dynamic history of 220 million years of subduction below Mexico: A correlation between slab geometry and overriding plate deformation based on geology, paleomagnetism, and seismic tomography. *Geochemistry, Geophysics, Geosystems*, *19*(12), 4649–4672. https://doi.org/10.1029/2018gc007739

Busby, C. (2004). Continental growth at convergent margins facing large ocean basins: A case study from Mesozoic convergent-margin basins of Baja California, Mexico. *Tectonophysics*, *392*(1–4), 241–277. https://doi.org/10.1016/j.tecto.2004.04.017

Busby, C., & Centeno-García, E. (2022). The "Nazas Arc" is a continental rift province: Implications for Mesozoic tectonic reconstructions of the southwest Cordillera, US and Mexico. *Geosphere*, *18*(2), 647–669. https://doi.org/10.1130/ges02443.1

Centeno-García, E. (2017). Mesozoic tectono-magmatic evolution of Mexico: An overview. *Ore Geology Reviews*, *81*, 1035–1052. https://doi.org/10.1016/j.oregeorev.2016.10.010

Chapman, A. D. (2017). The Pelona–Orocopia–Rand and related schists of southern California: A review of the best-known archive of shallow subduction on the planet. *International Geology Review*, *59*(5–6), 664–701. https://doi.org/10.1080/00206814.2016.1230836

Chapman, J. B. (2021). Diapiric relamination of the Orocopia Schist (southwestern US) during low-angle subduction. *Geology*, *49*(8), 983–987. https://doi.org/10.1130/g48647.1

Cloos, M. (1982). Flow melanges: Numerical modeling and geologic constraints on their origin in the Franciscan subduction complex, California. *Geological Society of America Bulletin*, *93*(4), 330–345. https://doi.org/10.1130/0016-7606(1982)93<330:fmnmag>2.0.co;2

Contreras-López, M., Delgado-Argote, L. A., Weber, B., Torres-Carrillo, X. G., Frei, D., Gómez-Alvarez, D. K., et al. (2021). Geochemistry, UPb geochronology, and Sr-Nd-Hf isotope systematics of a SW-NE transect in the southern Peninsular Ranges batholith, Mexico: Cretaceous magmatism developed on a juvenile island-arc crust. *Lithos*, *400*, 106375. https://doi.org/10.1016/j.lithos.2021.106375

Cordova, J. L., Mulcahy, S. R., Schermer, E. R., & Webb, L. E. (2019). Subduction initiation and early evolution of the Easton metamorphic suite, northwest Cascades, Washington. *Lithosphere*, *11*(1), 44–58. https://doi.org/10.1130/l1009.1

19449194, 2026, 4, Downloaded from https://agupubs.onlinelibrary.wiley.com/doi/10.1029/2025TC009340, Wiley Online Library on [01/06/2026]. See the Terms and Conditions (https://onlinelibrary.wiley.com/terms-and-conditions) on Wiley Online Library for rules of use; OA articles are governed by the applicable Creative Commons License

Corfu, F. (2003). Atlas of zircon textures. *Reviews in Mineralogy and Geochemistry*, *53*(1), 469–500. https://doi.org/10.2113/0530469

Coutts, D. S., Matthews, W. A., & Hubbard, S. M. (2019). Assessment of widely used methods to derive depositional ages from detrital zircon populations. *Geoscience Frontiers*, *10*(4), 1421–1435. https://doi.org/10.1016/j.gsf.2018.11.002

Cunetta, N. S., Mulcahy, S. R., Schermer, E. R., & Smit, M. A. (2025). Early Jurassic subduction initiation recorded in the Easton metamorphic suite, Northwest Cascades (Washington, USA). *Geological Society of America Bulletin*. https://doi.org/10.1130/B38167.1

Curray, J. R. (2005). Tectonics and history of the Andaman Sea region. *Journal of Asian Earth Sciences*, *25*(1), 187–232. https://doi.org/10.1016/j.jseaes.2004.09.001

DeCelles, P. G. (2004). Late Jurassic to Eocene evolution of the Cordilleran thrust belt and foreland basin system, western USA. *American Journal of Science*, *304*(2), 105–168. https://doi.org/10.2475/ajs.304.2.105

De Saint Blanquat, M., Tikoff, B., Teyssier, C., & Vigneresse, J. L. (1998). Transpressional kinematics and magmatic arcs. *Geological Society, London, Special Publications*, *135*(1), 327–340. https://doi.org/10.1144/gsl.sp.1998.135.01.21

Ding, L., Kapp, P., & Wan, X. (2005). Paleocene–Eocene record of ophiolite obduction and initial India-Asia collision, south central Tibet. *Tectonics*, *24*(3), 916. https://doi.org/10.1029/2004tc001729

Dumitru, T. A., Wakabayashi, J., Wright, J. E., & Wooden, J. L. (2010). Early Cretaceous transition from nonaccretionary behavior to strongly accretionary behavior within the Franciscan subduction complex. *Tectonics*, *29*(5). https://doi.org/10.1029/2009tc002542

Engebretson, D. C., Cox, A., & Gordon, R. G. (1984). Relative motions between oceanic plates of the Pacific basin. *Journal of Geophysical Research*, *89*(B12), 10291–10310. https://doi.org/10.1029/jb089ib12p10291

England, P., & Holland, T. (1979). Archimedes and the Tauern eclogites: The role of buoyancy in the preservation of exotic eclogite blocks. *Earth and Planetary Science Letters*, *44*(2), 287–294. https://doi.org/10.1016/0012-821x(79)90177-8

Ernst, W. G. (1971). Metamorphic zonations on presumably subducted lithospheric plates from Japan, California and the Alps. *Contributions to Mineralogy and Petrology*, *34*(1), 43–59. https://doi.org/10.1007/BF00376030

Ferrari, L., López-Martínez, M., Orozco-Esquivel, T., Bryan, S. E., Duque-Trujillo, J., Lonsdale, P., & Solari, L. (2013). Late Oligocene to Middle Miocene rifting and synextensional magmatism in the southwestern Sierra Madre Occidental, Mexico: The beginning of the Gulf of California rift. *Geosphere*, *9*(5), 1161–1200.

Festa, A., Pini, G. A., Ogata, K., & Dilek, Y. (2019). Diagnostic features and field-criteria in recognition of tectonic, sedimentary and diapiric mélanges in orogenic belts and exhumed subduction-accretion complexes. *Gondwana Research*, *74*, 7–30. https://doi.org/10.1016/j.gr.2019.01.003

Fossen, H., Teyssier, C., & Whitney, D. L. (2013). Transtensional folding. *Journal of Structural Geology*, *56*, 89–102. https://doi.org/10.1016/j.jsg.2013.09.004

Gehrels, G., & Pecha, M. (2014). Detrital zircon U-Pb geochronology and Hf isotope geochemistry of Paleozoic and Triassic passive margin strata of western North America. *Geosphere*, *10*(1), 49–65.

Gehrels, G. E., Valencia, V. A., & Ruiz, J. (2008). Enhanced precision, accuracy, efficiency, and spatial resolution of U-Pb ages by laser ablation–multicollector–inductively coupled plasma–mass spectrometry. *Geochemistry, Geophysics, Geosystems*, *9*(3). https://doi.org/10.1029/2007gc001805

Gerya, T. V., Stöckhert, B., & Perchuk, A. L. (2002). Exhumation of high-pressure metamorphic rocks in a subduction channel: A numerical simulation. *Tectonics*, *21*(6), 6-1–19. https://doi.org/10.1029/2002tc001406

Gonzalez, J. P., & Baldwin, S. L. (2019). Modelling white mica pressure-temperature-time (P-T-t) paths using thermobarometric and ^{40}Ar/^{39}Ar thermochronologic data. *Terra Nova*, *31*(3), 169–178. https://doi.org/10.1111/ter.12381

Goodge, J. (1995). Pre-Middle Jurassic accretionary metamorphism in the southern Klamath Mountains of northern California, USA. *Journal of Metamorphic Geology*, *13*(1), 93–110. https://doi.org/10.1111/j.1525-1314.1995.tb00207.x

Goodge, J. W. (1990). Tectonic evolution of a coherent Late Triassic subduction complex, Stuart Fork terrane, Klamath Mountains, northern California. *Geological Society of America Bulletin*, *102*(1), 86–101. https://doi.org/10.1130/0016-7606(1990)102<0086:teoacl>2.3.co;2

Grove, M., Jacobson, C. E., Barth, A. P., & Vucic, A. (2003). Temporal and spatial trends of Late Cretaceous-early Tertiary underplating Pelona and related schist beneath Southern California and southwestern Arizona.

Guilmette, C., Hébert, R., Dostal, J., Indares, A., Ullrich, T., Bédard, É., & Wang, C. (2012). Discovery of a dismembered metamorphic sole in the Saga ophiolitic mélange, South Tibet: Assessing an Early Cretaceous disruption of the Neo-Tethyan supra-subduction zone and consequences on basin closing. *Gondwana Research*, *22*(2), 398–414. https://doi.org/10.1016/j.gr.2011.10.012

Guilmette, C., Smit, M. A., van Hinsbergen, D. J., Gürer, D., Corfu, F., Charette, B., et al. (2018). Forced subduction initiation recorded in the sole and crust of the Semail Ophiolite of Oman. *Nature Geoscience*, *11*(9), 688–695. https://doi.org/10.1038/s41561-018-0209-2

Haq, S. S. (2012). Out-of-sequence thrusting in experimental Coulomb wedges: Implications for the structural development of mega-splay faults and forearc basins. *Geophysical Research Letters*, *39*(20). https://doi.org/10.1029/2012gl053176

Harvey, K. M., Penniston-Dorland, S. C., Kohn, M. J., & Piccoli, P. M. (2021). Assessing P-T variability in mélange blocks from the Catalina Schist: Is there differential movement at the subduction interface? *Journal of Metamorphic Geology*, *39*(3), 271–295. https://doi.org/10.1111/jmg.12571

Holt, A. F., & Condit, C. B. (2021). Slab temperature evolution over the lifetime of a subduction zone. *Geochemistry, Geophysics, Geosystems*, *22*(6), e2020GC009476. https://doi.org/10.1029/2020gc009476

Hopson, C. A., Mattinson, J. M., Pessagno, E. A., & Luyendyk, B. P. (2008). California Coast Range ophiolite: Composite middle and late Jurassic oceanic lithosphere.

Hopson, C. A., & Pessagno, E. A., Jr. (2005). Tehama-Colusa serpentinite mélange: A remnant of Franciscan Jurassic oceanic lithosphere, northern California. *International Geology Review*, *47*(1), 65–100. https://doi.org/10.2747/0020-6814.47.1.65

Hoskin, P. W., & Schaltegger, U. (2003). The composition of zircon and igneous and metamorphic petrogenesis. *Reviews in Mineralogy and Geochemistry*, *53*(1), 27–62. https://doi.org/10.2113/0530027

Isozaki, Y., Aoki, K., Nakama, T., & Yanai, S. (2010). New insight into a subduction-related orogen: A reappraisal of the geotectonic framework and evolution of the Japanese Islands. *Gondwana Research*, *18*(1), 82–105. https://doi.org/10.1016/j.gr.2010.02.015

Jiang, H., & Lee, C.-T. A. (2019). On the role of chemical weathering of continental arcs in long-term climate regulation: A case study of the Peninsular Ranges batholith, California (USA). *Earth and Planetary Science Letters*, *525*, 115733. https://doi.org/10.1016/j.epsl.2019.115733

Kimbrough, D. L. (1985). *Tectonostratigraphic terranes of the Vizcaino Peninsula and Cedros and San Benito Islands*. Baja California.

Kimbrough, D. L., & Moore, T. E. (2003). Ophiolite and volcanic arc assemblages on the Vizcaino Peninsula and Cedros Island, Baja California Sur, Mexico: Mesozoic forearc lithosphere of the Cordilleran magmatic arc. In *Special Papers—Geological Society of America* (pp. 43–72).

Kimbrough, D. L., Smith, D. P., Mahoney, J. B., Moore, T. E., Grove, M., Gastil, R. G., et al. (2001). Forearc-basin sedimentary response to rapid Late Cretaceous batholith emplacement in the Peninsular Ranges of southern and Baja California. *Geology*, *29*(6), 491–494. https://doi.org/10.1130/0091-7613(2001)029<0491:fbsrtr>2.0.co;2

19449194, 2026, 4, Downloaded from https://agupubs.onlinelibrary.wiley.com/doi/10.1029/2025TC009340, Wiley Online Library on [01/06/2026]. See the Terms and Conditions (https://onlinelibrary.wiley.com/terms-and-conditions) on Wiley Online Library for rules of use; OA articles are governed by the applicable Creative Commons License

Krohe, A. (2017). The Franciscan Complex (California, USA)—The model case for return-flow in a subduction channel put to the test. *Gondwana Research*, *45*, 282–307. https://doi.org/10.1016/j.gr.2017.02.003

Lee, J.-Y., Marti, K., Severinghaus, J. P., Kawamura, K., Yoo, H.-S., Lee, J. B., & Kim, J. S. (2006). A redetermination of the isotopic abundances of atmospheric Ar. *Geochimica et Cosmochimica Acta*, *70*(17), 4507–4512. https://doi.org/10.1016/j.gca.2006.06.1563

Malavieille, J., Molli, G., Genti, M., Dominguez, S., Beyssac, O., Taboada, A., et al. (2016). Formation of ophiolite-bearing tectono-sedimentary mélanges in accretionary wedges by gravity driven submarine erosion: Insights from analogue models and case studies. *Journal of Geodynamics*, *100*, 87–103. https://doi.org/10.1016/j.jog.2016.05.008

Maruyama, S., Liou, J. G., & Terabayashi, M. (1996). Blueschists and eclogites of the world and their exhumation. *International Geology Review*, *38*(6), 485–594. https://doi.org/10.1080/00206819709465347

Matthews, K. J., Maloney, K. T., Zahirovic, S., Williams, S. E., Seton, M., & Müller, R. D. (2016). Global plate boundary evolution and kinematics since the late Paleozoic. *Global and Planetary Change*, *146*, 226–250. https://doi.org/10.1016/j.gloplacha.2016.10.002

Menant, A., Angiboust, S., Gerya, T., Lacassin, R., Simoes, M., & Grandin, R. (2020). Transient stripping of subducting slabs controls periodic forearc uplift. *Nature Communications*, *11*(1), 1823. https://doi.org/10.1038/s41467-020-15580-7

Min, K., Mundil, R., Renne, P. R., & Ludwig, K. R. (2000). A test for systematic errors in ^{40}Ar/^{39}Ar geochronology through comparison with U/Pb analysis of a 1.1-Ga rhyolite. *Geochimica et Cosmochimica Acta*, *64*(1), 73–98. https://doi.org/10.1016/s0016-7037(99)00204-5

Morley, C. (1988). Out-of-sequence thrusts. *Tectonics*, *7*(3), 539–561. https://doi.org/10.1029/tc007i003p00539

Mulcahy, S. R., Starnes, J. K., Day, H. W., Coble, M. A., & Vervoort, J. D. (2018). Early onset of Franciscan subduction. *Tectonics*, *37*(5), 1194–1209. https://doi.org/10.1029/2017tc004753

Müller, R. D., Cannon, J., Qin, X., Watson, R. J., Gurnis, M., Williams, S., et al. (2018). GPlates: Building a virtual Earth through deep time. *Geochemistry, Geophysics, Geosystems*, *19*(7), 2243–2261. https://doi.org/10.1029/2018GC007584

Paces, J. B., & Miller Jr, J. D. (1993). Precise U-Pb ages of Duluth complex and related mafic intrusions, northeastern Minnesota: Geochronological insights to physical, petrogenetic, paleomagnetic, and tectonomagmatic processes associated with the 1.1 Ga midcontinent rift system. *Journal of Geophysical Research: Solid Earth*, *98*(B8), 13997–14013. https://doi.org/10.1029/93jb01159

Peacock, S. M. (1996). Thermal and petrologic structure of subduction zones. In *Subduction: Top to bottom* (Vol. 96, pp. 119–133).

Penniston-Dorland, S. C., Kohn, M. J., & Manning, C. E. (2015). The global range of subduction zone thermal structures from exhumed blueschists and eclogites: Rocks are hotter than models. *Earth and Planetary Science Letters*, *428*, 243–254. https://doi.org/10.1016/j.epsl.2015.07.031

Platt, J. P. (1975). Metamorphic and deformational processes in the Franciscan Complex, California: Some insights from the Catalina Schist terrane. *GSA Bulletin*, *86*(10), 1337–1347. https://doi.org/10.1130/0016-7606(1975)86<1337:Madpit>2.0.Co;2

Platt, J. P. (1986). Dynamics of orogenic wedges and the uplift of high-pressure metamorphic rocks. *Geological Society of America Bulletin*, *97*(9), 1037–1053. https://doi.org/10.1130/0016-7606(1986)97<1037:doowat>2.0.co;2

Platt, J. P. (1987). The uplift of high-pressure-low-temperature metamorphic rocks. *Philosophical Transactions of the Royal Society of London. Series A, Mathematical and Physical Sciences*, *321*(1557), 87–103. https://doi.org/10.1098/rsta.1987.0006

Plunder, A., Thieulot, C., & Van Hinsbergen, D. J. (2018). The effect of obliquity on temperature in subduction zones: Insights from 3-D numerical modeling. *Solid Earth*, *9*(3), 759–776. https://doi.org/10.5194/se-9-759-2018

Pullen, A., Ibáñez-Mejia, M., Gehrels, G. E., Giesler, D., & Pecha, M. (2018). Optimization of a laser ablation-single collector-inductively coupled plasma-mass spectrometer (Thermo element 2) for accurate, precise, and efficient Zircon U-Th-Pb geochronology. *Geochemistry, Geophysics, Geosystems*, *19*(10), 3689–3705. https://doi.org/10.1029/2018GC007889

Ramos-Velázquez, E., Calmus, T., Valencia, V., Iriondo, A., Valencia-Moreno, M., & Bellon, H. (2008). U-Pb and ^{40}Ar/^{39}Ar geochronology of the coastal Sonora batholith: New insights on Laramide continental arc magmatism. *Revista Mexicana de Ciencias Geológicas*, *25*(2), 314–333.

Rangin, C. (1978). Speculative model of Mesozoic geodynamics, central Baja California to northeastern Sonora (Mexico).

Rangin, C. (1979). Tectónicas sobrepuestas en Sonora septentrional. In P. L. Abbott & R. G. Gastil (Eds.), *Evidence for superimposed subduction and collision processes during Jurassic-Cretaceous time along Baja California continental borderland* (pp. 37–51).

Ring, U., & Brandon, M. T. (1999). Ductile deformation and mass loss in the Franciscan subduction complex: Implications for exhumation processes in accretionary wedges. *Geological Society, London, Special Publications*, *154*(1), 55–86. https://doi.org/10.1144/gsl.sp.1999.154.01.03

Ross, J. (2017). *Pychron documentation*. New Mexico Institute of Mining and Technology.

Ruh, J. B. (2020). Numerical modeling of tectonic underplating in accretionary wedge systems. *Geosphere*, *16*(6), 1385–1407. https://doi.org/10.1130/ges02273.1

Rutte, D., Garber, J., Kylander-Clark, A., & Renne, P. R. (2020). An exhumation pulse from the nascent Franciscan subduction zone (California, USA). *Tectonics*, *39*(10), e2020TC006305. https://doi.org/10.1029/2020tc006305

Schaen, A. J., Jicha, B. R., Hodges, K. V., Vermeesch, P., Stelten, M. E., Mercer, C. M., et al. (2021). Interpreting and reporting ^{40}Ar/^{39}Ar geochronologic data. *Bulletin*, *133*(3–4), 461–487. https://doi.org/10.1130/b35560.1

Schweickert, R. A., & Cowan, D. S. (1975). Early Mesozoic tectonic evolution of the western Sierra Nevada, California. *Geological Society of America Bulletin*, *86*(10), 1329–1336. https://doi.org/10.1130/0016-7606(1975)86<1329:emteot>2.0.co;2

Sedlock, R. L. (1988a). *Lithology, petrology, structure, and tectonics of blueschists and associated rocks, west-central Baja California, Mexico*. Stanford University.

Sedlock, R. L. (1988b). Metamorphic petrology of a high-pressure, low-temperature subduction complex in west-central Baja California, Mexico. *Journal of Metamorphic Geology*, *6*(2), 205–233. https://doi.org/10.1111/j.1525-1314.1988.tb00416.x

Sedlock, R. L. (1988c). Tectonic setting of blueschist and island-arc terranes of west-central Baja California, Mexico. *Geology*, *16*(7), 623–626. https://doi.org/10.1130/0091-7613(1988)016<0623:tsobai>2.3.co;2

Sedlock, R. L. (1996). Syn-Subduction Forearc extension and blueschist exhumation in Baja California, México. In *Subduction* (pp. 155–162). https://doi.org/10.1029/GM096p0155

Sedlock, R. L. (2003). Four phases of mesozoic deformation in the sierra de san andres ophiolite, vizcaino peninsula, west-central baja California, Mexico.

Sedlock, R. L., & Isozaki, Y. (1990). Lithology and biostratigraphy of franciscan-like chert and associated rocks in west-central Baja California, Mexico. *Geological Society of America Bulletin*, *102*(7), 852–864. https://doi.org/10.1130/0016-7606(1990)102<0852:labofl>2.3.co;2

Sharman, G. R., Sharman, J. P., & Sylvester, Z. (2018). detritalPy: A python-based toolset for visualizing and analysing detrital geo-thermochronologic data. *Depositional Record*, *4*(2), 202–215. https://doi.org/10.1002/dep2.45

Shervais, J. W. (2001). Birth, death, and resurrection: The life cycle of suprasubduction zone ophiolites. *Geochemistry, Geophysics, Geosystems*, *2*(1). https://doi.org/10.1029/2000gc000080

19449194, 2026, 4, Downloaded from https://agupubs.onlinelibrary.wiley.com/doi/10.1029/2025TC009340, Wiley Online Library on [01/06/2026]. See the Terms and Conditions (https://onlinelibrary.wiley.com/terms-and-conditions) on Wiley Online Library for rules of use; OA articles are governed by the applicable Creative Commons License

Shervais, J. W., Choi, S. H., Sharp, W. D., Ross, J., Zoglman-Schuman, M., Mukasa, S. B., et al. (2011). Serpentinite matrix mélange: Implications of mixed provenance for mélange formation. In *Mélanges: Processes of formation and societal significance* (Vol. 480). Geological Society of America. https://doi.org/10.1130/2011.2480(01)

Shervais, J. W., Murchey, B. L., Kimbrough, D. L., Renne, P. R., & Hanan, B. (2005). Radioisotopic and biostratigraphic age relations in the Coast Range Ophiolite, northern California: Implications for the tectonic evolution of the Western Cordillera. *Geological Society of America Bulletin*, *117*(5–6), 633–653. https://doi.org/10.1130/b25443.1

Smith, D. P., & Busby, C. J. (1993). Mid-Cretaceous crustal extension recorded in deep-marine half-graben fill, Cedros Island, Mexico. *Geological Society of America Bulletin*, *105*(4), 547–562. https://doi.org/10.1130/0016-7606(1993)105<0547:mcceri>2.3.co;2

Stern, R. J., & Bloomer, S. H. (1992). Subduction zone infancy: Examples from the Eocene Izu-Bonin-Mariana and Jurassic California arcs. *Geological Society of America Bulletin*, *104*(12), 1621–1636. https://doi.org/10.1130/0016-7606(1992)104<1621:szieft>2.3.co;2

Sundell, K. E., Gehrels, G. E., & Pecha, M. E. (2021). Rapid u-pb geochronology by laser Ablation Multi-collector ICP-MS. *Geostandards and Geoanalytical Research*, *45*(1), 37–57. https://doi.org/10.1111/ggr.12355

Teyssier, C., Whitney, D. L., Toraman, E., & Seaton, N. C. (2010). Lawsonite vorticity and subduction kinematics. *Geology*, *38*(12), 1123–1126. https://doi.org/10.1130/g31409.1

Tsujimori, T., & Ernst, W. (2014). Lawsonite blueschists and lawsonite eclogites as proxies for palaeo-subduction zone processes: A review. *Journal of Metamorphic Geology*, *32*(5), 437–454. https://doi.org/10.1111/jmg.12057

van Keken, P. E., Wada, I., Abers, G. A., Hacker, B. R., & Wang, K. (2018). Mafic high-pressure rocks are preferentially exhumed from warm subduction settings. *Geochemistry, Geophysics, Geosystems*, *19*(9), 2934–2961. https://doi.org/10.1029/2018gc007624

van Keken, P. E., & Wilson, C. R. (2023). An introductory review of the thermal structure of subduction zones: I—Motivation and selected examples. *Progress in Earth and Planetary Science*, *10*(1), 42. https://doi.org/10.1186/s40645-023-00573-z

Vermeesch, P. (2018). IsoplotR: A free and open toolbox for geochronology. *Geoscience Frontiers*, *9*(5), 1479–1493. https://doi.org/10.1016/j.gsf.2018.04.001

Vermeesch, P. (2021). Maximum depositional age estimation revisited. *Geoscience Frontiers*, *12*(2), 843–850. https://doi.org/10.1016/j.gsf.2020.08.008

Wakabayashi, J. (1999). Subduction and the rock record: Concepts developed in the Franciscan complex.

Wakabayashi, J. (2015). Anatomy of a subduction complex: Architecture of the Franciscan Complex, California, at multiple length and time scales. *International Geology Review*, *57*(5–8), 669–746. https://doi.org/10.1080/00206814.2014.998728

Wakabayashi, J. (2017). Structural context and variation of ocean plate stratigraphy, Franciscan Complex, California: Insight into mélange origins and subduction-accretion processes. *Progress in Earth and Planetary Science*, *4*(1), 1–23. https://doi.org/10.1186/s40645-017-0132-y

Wakabayashi, J. (2019). Sedimentary compared to tectonically-deformed serpentinites and tectonic serpentinite mélanges at outcrop to petrographic scales: Unambiguous and disputed examples from California. *Gondwana Research*, *74*, 51–67. https://doi.org/10.1016/j.gr.2019.04.005

Wakabayashi, J. (2025). Mind the matrix: Criteria to evaluate whether mélange matrix formed as a clastic sedimentary rock or as a fault zone.

Wakabayashi, J., Shimabukuro, D., Masutsubo, N., Eck, D., Spencer, S., Kemp, C., et al. (2023). Northern Sierra Nevada, California: Ophiolites, metamorphic soles, and blueschists to active tectonics and geomorphology.

Wakabayashi, J., Wakabayashi, J., & Dilek, Y. (2011). Mélanges of the Franciscan Complex, California: Diverse structural settings, evidence for sedimentary mixing, and their connection to subduction processes. In *Melanges: Processes of formation and societal significance* (Vol. 480). Geological Society of America. https://doi.org/10.1130/2011.2480(05)

Wang, J. W., Gehrels, G., Kapp, P., & Sundell, K. (2022). Evidence for regionally continuous Early Cretaceous sinistral shear zones along the western flank of the Coast Mountains, coastal British Columbia, Canada. *Geosphere*, *19*(1), 139–162. https://doi.org/10.1130/ges02502.1

Wang, J. W., Kapp, P., Holder, R., He, J., Hernandez-Uribe, D., & Worthington, J. (2026). Polycyclic metamorphism, exhumation, and recycling of subduction complex rocks, Cedros island, Baja California. *Zenodo*. https://doi.org/10.5281/zenodo.17978619

Wickham, H. (2016). ggplot2: Elegant graphics for data analysis. Springer-Verlag New York.

Žák, J., Svojtka, M., Hajná, J., & Ackerman, L. (2020). Detrital zircon geochronology and processes in accretionary wedges. *Earth-Science Reviews*, *207*, 103214.

19449194, 2026, 4, Downloaded from https://agupubs.onlinelibrary.wiley.com/doi/10.1029/2025TC009340, Wiley Online Library on [01/06/2026]. See the Terms and Conditions (https://onlinelibrary.wiley.com/terms-and-conditions) on Wiley Online Library for rules of use; OA articles are governed by the applicable Creative Commons License